Above-threshold ionization in multicenter molecules: The role of the initial state

Noslen Suárez,[1,*] Alexis Chacón,[2] Emilio Pisanty,[1] Lisa Ortmann,[3] Alexandra S. Landsman,[3,4] Antonio Picón,[1,5,†] Jens Biegert,[1,6] Maciej Lewenstein,[1,6] and Marcelo F. Ciappina[7]

[1]*Institut de Ciencies Fotoniques, The Barcelona Institute of Science and Technology, 08860 Castelldefels, Barcelona, Spain*
[2]*Theoretical Division, Los Alamos National Laboratory, Los Alamos, New Mexico 87545, USA*
[3]*Max-Planck Institut für Physik komplexer Systeme, Nöthnitzer-Strasse 38, D-01187 Dresden, Germany*
[4]*Department of Physics, Max Planck Postech, Pohang, Gyeongbuk 37673, Republic of Korea*
[5]*Grupo de Investigación en Aplicaciones del Láser y Fotónica, Departamento de Física Aplicada, University of Salamanca, 37008 Salamanca, Spain*
[6]*ICREA, Pg. Lluís Companys 23, 08010 Barcelona, Spain*
[7]*Institute of Physics of the ASCR, ELI-Beamlines Project, Na Slovance 2, 182 21 Prague, Czech Republic*

(Received 13 September 2017; published 29 March 2018)

A possible route to extract electronic and nuclear dynamics from molecular targets with attosecond temporal and nanometer spatial resolution is to employ recolliding electrons as "probes." The recollision process in molecules is, however, very challenging to treat using *ab initio* approaches. Even for the simplest diatomic systems, such as H_2, today's computational capabilities are not enough to give a complete description of the electron and nuclear dynamics initiated by a strong laser field. As a consequence, approximate qualitative descriptions are called to play an important role. In this paper we extend the work presented in Suárez *et al.* [N. Suárez, A. Chacón, J. A. Pérez-Hernández, J. Biegert, M. Lewenstein, and M. F. Ciappina, High-order-harmonic generation in atomic and molecular systems, Phys. Rev. A **95**, 033415 (2017)] to three-center molecular targets. Additionally, we incorporate a more accurate description of the molecular ground state, employing information extracted from quantum chemistry software packages. This step forward allows us to include, in a detailed way, both the molecular symmetries and nodes present in the high-occupied molecular orbital. We are able, on the one hand, to keep our formulation as analytical as in the case of diatomics and, on the other hand, to still give a complete description of the underlying physics behind the above-threshold ionization process. The application of our approach to complex multicenter—with more than three centers—targets appears to be straightforward.

DOI: 10.1103/PhysRevA.97.033415

I. INTRODUCTION

Strong-field techniques such as high-order-harmonic spectroscopy (HHS) are the workhorses for one of the most stimulating prospects of strong-field and attosecond physics: the extraction of electronic and nuclear information on the attosecond temporal and subangstrom spatial scales using recolliding electrons as "probes." HHS employs the quiver motion of an electron, which is liberated by the laser field from the target structure itself, to analyze either the recombination spectrum or the momentum distribution of the rescattering electron.

For instance, the Dyson orbital of an N_2 molecule was reconstructed with tomographic techniques, using the information contained in the high-order-harmonic generation (HHG) spectrum [1]. The original interpretation of these experiments relies on the strong-field approximation (SFA), which provides a fully quantum description of the well-known "three-step model." Later on, Itatani *et al.*'s [2] experiment sparked a true avalanche of experimental and theoretical work on the subject. The use of approximations in the theoretical modeling of HHG in molecules (and in particular the SFA) is, however, not exempt from controversies: the results strongly rely upon the specifics of the model, namely, the gauge, the choice of the dipole radiation form, the molecular orbital (MO) symmetry and degree of alignment, etc. (see [3–11]).

One step forward in the extraction of molecular structural features is provided by the so-called laser-induced electron diffraction (LIED) [12–14] technique. Here, the recolliding electrons, elastically scattered off the molecular ion, contain information about the multicenter nature of the target that can be easily extracted from the measured photoelectron spectra. Currently, LIED has been used to successfully recover structural information from diatomic and other polyatomic molecules with subangstrom spatial resolution. LIED is based on the above-threshold ionization (ATI) processes. In ATI an electron may directly depart from the molecular target and contribute to the lower-energy region ATI spectrum; this process is termed direct tunneling. On the other hand, the laser-ionized electron might return to the vicinity of the molecular parent ion, driven by the still present laser electric field, and rescatter, thereby gaining much more kinetic energy. This highly energetic electron could excite the remaining ion or even cause the detachment of another electron(s) (for a comprehensive description of these processes within the framework of the SFA and Feynman's path-integral approach, see, e.g., [15]).

*noslen.suarez@icfo.es
†Present address: Departamento de Química, C-9, Universidad Autónoma de Madrid, 28049 Madrid, Spain.

The viability of LIED as a self-imaging technique—the probe is a molecular electron that is extracted from the same target it images—has been already established in a series of contributions [16–19]. The aim is to gain insight about the electronic structure of complex molecular targets interpreting the energy spectra and angular distribution of ATI electrons. Specifically, the high-energy region of the ATI spectra, which is governed by the rescattering process, is particularly sensitive to the structure and features of the target. In other words, the rescattered electron has acquired knowledge about the target it rescattered off, and hence allows extracting structural information.

The study of the structure of complex systems, such as molecules, atomic clusters, and solids, using the ATI spectra is a well developed area of research. In this regard, ATI from the simplest molecular systems, i.e., diatomics, is one the most widely studied processes. Usually, theoretical approaches can be divided in two main groups: those based on a fully quantum-mechanical description, that rely upon on the numerical solution of the time-dependent Schrödinger equation (TDSE), and approximate methods based on the SFA and similar quasiclassical approaches. We should mention, however, that the solution of the TDSE within the so-called single active electron (SAE) approximation is only viable for the simplest diatomic molecules, e.g., H_2^+, H_2, and D_2. These quantum-mechanical results so far largely focused on the discrepancies between the length and velocity gauge outcomes [20], the influence of the internuclear distance in the interference patterns [21], or how the molecular alignment [13,22–26] affects the ATI photoelectron or HHG spectra. Finally, the importance of the residual Coulomb interaction and quality of the continuum electron wave function was also assessed [27,28]. Even though the TDSE provides the most accurate and complete description of the underlying physics behind ATI and LIED, its numerical integration is very expensive computationally speaking. Furthermore, the TDSE in its full dimensionality can currently not be solved for complex molecular targets and multielectron systems. Additionally, it is still not possible to model the time evolution of molecular systems with the required temporal resolution. Thus, approximate descriptions such as the SFA and related methods play a fundamental role in the adequate description of the more complex instances of LIED and ATI. Similarly, the SFA approach is instrumental in the interpretation of HHG molecular tomography.

We already presented a general theory for symmetric diatomic molecules in the SAE approximation that, among other features, allows adjusting both the internuclear separation and molecular potential in a direct and simple way [29]. Such approach relies upon an analytic approximate solution of the TDSE and is based on a modified version of SFA. Using that approach, we were able to find expressions for direct and rescattered electron transition amplitudes from two-center molecular systems. In addition, our model directly underpins different underlying physical processes (see, e.g., [29–31]). Two important advantages of our theory are that (i) the dipole matrix elements are free from nonphysical gauge and coordinate system-dependent terms—this is achieved by adapting the coordinate system, in which SFA is performed, to the center from which the corresponding part of the time-dependent wave function originates—and (ii) we are able to write both the direct and rescattering transition amplitudes in an analytical form, only involving one-dimensional and two-dimensional time integrals, respectively.

Before proceeding, we would like stress once more the essence of our approach. SFA in the formulation of Lewenstein *et al.* [32] is an approximate method to solve the TDSE, in which the contributions of all excited bound states are neglected, whereas continuum-continuum scattering processes are treated in the systematic perturbative way. In the zeroth order, dynamics (quasiclassical action) of electrons is the same as for Volkov electrons. In the first order, momentum changing electron scattering processes in the presence of the laser field are included. But, the matrix elements for the dipole transition and for the continuum-continuum transition are calculated using the exact ground-state wave function and exact continuum states, corresponding to outgoing electrons of a fixed outgoing momentum. These wave functions form an orthonormal, although not complete (due to the exclusion of the excited bound states), set. In particular, continuum states in such approach "know" about the spatial position and structure of the target in question: an atom, a molecule, or a solid state. For technical reasons, in many applications plane waves are used to describe the continuum states—many researches associate that with the standard SFA approach. For us it is an additional approximation, which might lead to unnecessary problems in calculations. Plane waves form themselves an orthonormal basis, and thus are not orthogonal to the ground state. This fact causes the appearance of unphysical, and particularly large, contributions to the dipole moment matrix elements. In [31] we have illustrated this in the context of diatomic molecules and we have also presented some comparisons of our approach with the TDSE—we refer the reader to the discussion therein.

We emphasize that our proposed theory of adapting the coordinate system in multicenter targets is better than the standard SFA, in which plane waves are used. This is the case especially if the target size is large, but it is also true when the typical internuclear distances near the equilibrium are small. We checked that spurious terms, appearing due to the lack of orthogonality between the ground state and continuum plane waves, are of the same order as the nonspurious contributions. This does not mean, obviously, that the standard SFA applied to diatomic molecules, using a single coordinate system, centered at the center of the molecule, as studied in [24,33], is of no worth. It gives the same results for the quasiclassical actions, and the same information about the quasiclassical trajectories, in particular the novel one connecting two different centers. Therefore, the most important exponential part of the formulas is the same, but the prefactors may substantially differ.

In the present paper we build on the theory presented in [29], namely, (a) extending the approach to three-center molecular systems and (b) including a more accurate description of the molecular ground state. For (b) a linear combination of atomic orbitals (LCAO), obtained from chemical software suites, is used to model the molecular high-occupied molecular orbital (HOMO). In principle, our approach is capable to manage any basis set, but in order to keep the formulation as analytical as possible we employ throughout the paper a STO-3G basis set.

This paper is organized as follows. In Sec. II, we present the formulas for the three-center molecular system ATI transition amplitudes for both direct and rescattered electrons. In Sec. III we describe how to obtain the bound-free dipole transition

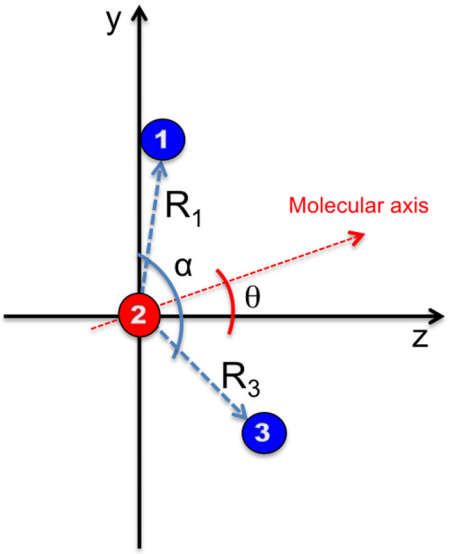

FIG. 1. A general three-center molecular system aligned at a θ angle with respect to the laser field polarization. The red dashed line defines the molecular axis (see text for details).

matrix element, with the molecular ground state approximated as a LCAO and using a STO-3G basis set. Details of the calculation of the rescattering electron states and the matrix elements that describe the continuum-continuum process are provided in an analytic form. We use the transition matrix elements obtained in the previous sections (Secs. II and III) in Sec. IV to compute photoelectron spectra for diatomic and triatomic molecules. Here, the numerical results retrieved using LCAO approach are compared with those obtained employing the nonlocal short-range (SR) potential. Finally, in Sec. VI, we summarize the main ideas, present our conclusions, and give a brief outlook.

II. THEORY OF ATI FOR A THREE-CENTER MOLECULAR SYSTEM

To obtain the transition probability amplitudes for a triatomic molecule within the modified strong-field approximation (MSFA), we extend the analysis presented in our previous works [29–31]. To this end, we start solving the TDSE for a molecular system of three independent atoms, as is shown in Fig. 1, under the influence of an intense and short laser pulse $\mathbf{E}(t)$, linearly polarized along the z axis.

Our molecular system is defined by a relative position vector $\mathbf{R} = \mathbf{R}_3 - \mathbf{R}_1$. We consider the general case of a molecule with different atoms placed at $\mathbf{R}_1 = [0, \frac{R}{2}\sin(\frac{\alpha}{2}+\theta), \frac{R}{2}\cos(\frac{\alpha}{2}+\theta)]$, $\mathbf{R}_2 = 0$, and $\mathbf{R}_3 = [0, -\frac{R}{2}\sin(\frac{\alpha}{2}-\theta), \frac{R}{2}\cos(\frac{\alpha}{2}-\theta)]$, where α and θ are the angles between the external atoms and the one formed by the molecular axis and the laser electric field polarization, respectively (see Fig. 1). The molecular axis is defined starting at the origin and bisecting the α angle. A model defined in this way is able to accommodate both linear and angular molecules. For the case of linear configurations $\alpha = 180^\circ$. Additionally, our approach allows one to study both fixed and randomly oriented molecules (for details see, e.g., [29–31]).

In general, as the molecular nuclei are much heavier than the electrons and the laser pulse duration is shorter than the nuclei vibration and rotational dynamics, we fix the nuclei positions and neglect the repulsive interaction between them. Further, throughout the formulation we consider the SAE approximation.

A. Generalized SFA: Transition probability amplitudes

We will work in the tunneling regime where our MSFA becomes valid [32,34–38]. We assume that the atomic potential $V(\mathbf{r})$ does not play an important role in the electron dynamics once the electron is freed and moving in the laser continuum. Following these observations, we further consider that (i) only the ground, $|0\rangle$, and continuum, $|\mathbf{v}\rangle$, states are taken into account in the interaction process; (ii) there is no depletion of the ground state ($U_p < U_{\rm sat}$); and (iii) the continuum states are approximated by Volkov states—in the continuum the electron is considered as a free particle entirely moving driven by the laser electric field. For a more detailed discussion of the validity of the above statements see, e.g., [29–32,38].

Based on assertions (i) and (ii), we propose a final state, that is a superposition of three atomic states as

$$|\Psi(t)\rangle = e^{iI_p t}\sum_{j=1}^{3}\left[|0_j\rangle + \int d^3\mathbf{v}\, b_j(\mathbf{v},t)|\mathbf{v}\rangle\right], \qquad (1)$$

constructed as a coherent superposition of ground, $|0\rangle = \sum_{j=1}^{3}|0_j\rangle$, and continuum, $|\mathbf{v}\rangle$, states [32,38]. The subscript $j = 1,2,3$ refers to the positions $\mathbf{R}_1$, $\mathbf{R}_2$, and $\mathbf{R}_3$ of each atom in the three-center molecule, respectively.

The prefactor $e^{iI_p t}$ represents the phase oscillations which describe the accumulated electron energy in the ground state ($I_p = -E_0$ is the ionization potential of the molecular target, with E_0 the ground-state energy of the three-center molecular system). Atomic units are used throughout this paper unless otherwise stated.

Solving the TDSE that governs all the laser-molecule interactions we find individual equations for the transition amplitudes $b_j(\mathbf{v},t)$ as

$$\begin{aligned}\dot{b}_j(\mathbf{v},t) = &-i\left(\frac{\mathbf{v}^2}{2} + I_p - \mathbf{R}_j\cdot\mathbf{E}(t)\right)b_j(\mathbf{v},t) + i\mathbf{E}(t)\cdot\mathbf{d}_j(\mathbf{v})\\ &+\mathbf{E}(t)\cdot\nabla_{\mathbf{v}}b_j(\mathbf{v},t)\\ &-i\mathbf{E}(t)\cdot\int d^3\mathbf{v}'\, b_j(\mathbf{v}',t)\,\mathbf{g}(\mathbf{v},\mathbf{v}'). \qquad (2)\end{aligned}$$

Notice that in Eq. (2) we included a correction depending on the relative position of each of the atoms $\mathbf{R}_j$. This adjustment allows us to build matrix elements free of nonphysical gauge and coordinate system-dependent contributions (see [29,31] for more details).

The first term on the right-hand side of Eq. (2) represents the phase evolution of the electron in the oscillating laser electric field. Here the linear term on $\mathbf{R}_j$ is introduced within the correction of the continuum-continuum transition matrix element $\mathbf{G}(\mathbf{v},\mathbf{v}') = \langle\mathbf{v}|(\mathbf{r}-\mathbf{R}_j)|\mathbf{v}'\rangle$ that relies upon the scattering states $|\mathbf{v}\rangle$ and $|\mathbf{v}'\rangle$ as

$$\mathbf{G}(\mathbf{v},\mathbf{v}') = i\,\nabla_{\mathbf{v}}\delta(\mathbf{v}-\mathbf{v}') - \mathbf{R}_j\delta(\mathbf{v}-\mathbf{v}') + \mathbf{g}(\mathbf{v},\mathbf{v}'). \qquad (3)$$

With the second term of Eq. (2) we define the bound-free transition matrix element: $\mathbf{d}_j(\mathbf{v}) = -\langle \mathbf{v}_p|(\mathbf{r}-\mathbf{R}_j)|0_j\rangle = -\langle \mathbf{v}_p|\mathbf{r}|0_j\rangle + \mathbf{R}_j\langle \mathbf{v}_p|0_j\rangle$.

The first two terms on the right-hand side of Eq. (3) are associated to events where the laser-ionized electron is accelerated by the laser electric field without probability of returning close to any of the ion cores and rescatters. The last one, the rescattering transition matrix element $\mathbf{g}(\mathbf{v},\mathbf{v}')$, accounts for all the continuum-continuum processes concerning the entire molecule. Thus, in $\mathbf{g}(\mathbf{v},\mathbf{v}')$ the residual Coulomb potential has to be taken into account. In this sense it can be written as a sum of components representing each rescattering channel on the molecule. The second term of Eq. (3) then reads as

$$\begin{aligned}\mathbf{g}(\mathbf{v},\mathbf{v}') = {} & \langle \mathbf{v}_p|(\mathbf{r}-\mathbf{R}_1)|\delta\mathbf{v}'_1\rangle + \langle \delta\mathbf{v}_1|(\mathbf{r}-\mathbf{R}_1)|\mathbf{v}'_p\rangle \\ & + \langle \mathbf{v}_p|(\mathbf{r}-\mathbf{R}_2)|\delta\mathbf{v}'_2\rangle + \langle \delta\mathbf{v}_2|(\mathbf{r}-\mathbf{R}_2)|\mathbf{v}'_p\rangle \\ & + \langle \mathbf{v}_p|(\mathbf{r}-\mathbf{R}_3)|\delta\mathbf{v}'_3\rangle + \langle \delta\mathbf{v}_3|(\mathbf{r}-\mathbf{R}_3)|\mathbf{v}'_p\rangle. \quad (4)\end{aligned}$$

B. Direct transition amplitude

To find the direct transition amplitude we use perturbation theory over $\mathbf{g}(\mathbf{v},\mathbf{v}')$ in order to solve the partial differential equation Eq. (2). The zeroth-order solution $b_0(\mathbf{v},t)$ corresponds to the direct transition amplitude describing processes where the laser-ionized electron goes to the continuum and never returns to the vicinity of the molecule, i.e., there is no rescattering with the remaining molecular ion. Therefore, $b_0(\mathbf{v},t)$ in terms of the canonical momentum $\mathbf{p} = \mathbf{v} - \mathbf{A}(t)$ can be written as

$$\begin{aligned}b_0(\mathbf{p},t) = i\sum_{j=1}^{3}\int_0^t dt'\, \mathbf{E}(t')\cdot\mathbf{d}_j[\mathbf{p}+\mathbf{A}(t')] \\ \times \exp[-i\, S_j(\mathbf{p},t,t')]. \quad (5)\end{aligned}$$

Equation (5) has a direct physical interpretation: it can be understood as the sum of all the ionization events that occur from the time t' to t in the entire molecule. Then, the instantaneous transition probability amplitude of an electron at a time t', at which it appears in the continuum with momentum $\mathbf{v}(t') = \mathbf{v} - \mathbf{A}(t) + \mathbf{A}(t') = \mathbf{p} + \mathbf{A}(t')$, is defined by the argument of the time integral in Eq. (5) [note that $\mathbf{A}(t) = -\int^t \mathbf{E}(t')dt'$ is the associated vector potential]. Furthermore, the exponent phase factor in Eq. (5) stands for the "semiclassical action" and reads as

$$S_j(\mathbf{p},t,t') = \mathbf{R}_j\cdot[\mathbf{A}(t)-\mathbf{A}(t')] + S(\mathbf{p},t,t'), \quad (6)$$

that defines a possible electron trajectory from the birth time t', at position $\mathbf{R}_j$, until the "recombination" one t; $S(\mathbf{p},t,t') = \int_{t'}^{t} d\tilde{t}\{[\mathbf{p}+\mathbf{A}(\tilde{t})]^2/2 + I_p\}$ is the well-known semiclassical action.

C. Rescattering transition amplitude

On the other hand, the first-order solution $b_1(\mathbf{v},t)$ refers to an electron that, once ionized at a particular center, has a certain probability of rescattering with each of the remaining ions (including the one from which it was laser ionized). In order to find the first-order correction, i.e., the transition amplitude for the rescattered photoelectrons $b_1(\mathbf{v},t)$, we set now $\mathbf{g}(\mathbf{v},\mathbf{v}') \neq \mathbf{0}$ in Eq. (2) and use the zeroth-order solution. The rescattering transition amplitude reads as

$$\begin{aligned}b_{1,jj'}(\mathbf{p},t) = -\int_0^t dt'\int_0^{t'} dt''\int d^3\mathbf{p}' \\ \times \mathbf{E}(t')\cdot\mathbf{g}_{jj'}[\mathbf{p}+\mathbf{A}(t'),\mathbf{p}'+\mathbf{A}(t')]\exp[-iS_{j'}(\mathbf{p},t,t')] \\ \times \mathbf{E}(t'')\cdot\mathbf{d}_j[\mathbf{p}'+\mathbf{A}(t'')]\exp[-iS_j(\mathbf{p}',t',t'')]. \quad (7)\end{aligned}$$

Notice that we have a three-center molecule where ionization and rescattering processes can take place at each of the individual atoms. In this sense we can distinguish between (i) $j = j'$, the local rescattering processes, which are "spatially localized" since the electron undergoes a local rescattering with the same atomic core from which it was born, and (ii) $j \neq j'$, for the nonlocal and cross ones, involving transition between two atoms.

The total rescattering transition amplitude, containing information about all the possible rescattering scenarios, is then formed by nine terms $b_1(\mathbf{p},t) = \sum_{j,j'=1}^{3} b_{1,jj'}(\mathbf{v},t)$: three local terms and six nonlocal and cross terms.

Equation (7) has a clear physical interpretation. As expected the rescattering transition amplitude contains two exponential factors, each representing the electron excursions in the laser continuum. The last factor in Eq. (7), $\exp[-iS_j(\mathbf{p}',t',t'')]$, represents the accumulated phase of an electron born at the time t'' in $\mathbf{R}_j$ until it rescatters at time t'. In the same way $\exp[-iS_{j'}(\mathbf{p},t,t')]$ defines the accumulated phase of the electron after it rescatters at a time t' to the "final" one t, when the electron is "measured" at the detector with momentum $\mathbf{p}$. Furthermore, the quantity $\mathbf{E}(t'')\cdot\mathbf{d}_j[\mathbf{p}'+\mathbf{A}(t'')]$ is the probability amplitude of an emitted electron at the time t'' that has a kinetic momentum of $\mathbf{v}'(t'') = \mathbf{p}' + \mathbf{A}(t'')$. Finally, the term $\mathbf{E}(t')\cdot\mathbf{g}_{jj'}[\mathbf{p}+\mathbf{A}(t'),\mathbf{p}'+\mathbf{A}(t')]$ defines the probability amplitude of rescattering at time t'.

The rescattering transition amplitude defined in Eq. (7) is a multidimensional highly oscillatory integral: a two-dimensional (2D) time integral embedded in a three-dimensional (3D) momentum integral. As a way to reduce the computational cost we shall employ the stationary phase method to partially evaluate it. We only take the contributions to the momentum integral at the saddle or stationary points $\mathbf{p}'_s$, which are obtained from the equation $\nabla_{\mathbf{p}'}S(\mathbf{p}')|_{\mathbf{p}'_s} = \mathbf{0}$. The latter equation implies $\mathbf{p}'_s = -\frac{1}{\tau}\int_{t''}^{t'}\mathbf{A}(\tilde{t})\mathbf{d}\tilde{t}$, where $\tau = t'-t''$ defines the excursion time of the electron in the laser continuum.

Therefore, applying the standard saddle-point method to the 3D momentum integral we obtain an expression for rescattering transition amplitude $b_{1,jj'}(\mathbf{p},t)$ as

$$\begin{aligned}b_{1,jj'}(\mathbf{p},t) = -\int_0^t dt'\int_0^{t'} dt''\left(\frac{\pi}{\varepsilon+\frac{i(t'-t'')}{2}}\right)^{\frac{3}{2}} \\ \times \mathbf{E}(t')\cdot\mathbf{g}_{jj'}[\mathbf{p}+\mathbf{A}(t'),\mathbf{p}'_s+\mathbf{A}(t')] \\ \times \exp[-iS_{j'}(\mathbf{p},t,t')]\,\mathbf{E}(t'')\cdot\mathbf{d}_j[\mathbf{p}'_s+\mathbf{A}(t'')] \\ \times \exp[-iS_j(\mathbf{p}'_s,t',t'')]. \quad (8)\end{aligned}$$

Here, we have introduced an infinitesimal parameter ε, small but nonzero, to avoid the divergence at $t' = t''$. The character of this not integrable singularity and the simple method to handle it has been pioneered in [32]. For more information see the discussion in [30].

The total photoelectron spectra at the end of the laser pulse t_F, $|b(\mathbf{p},t_F)|^2$, is then a coherent superposition of both the direct $b_0(\mathbf{p},t_F)$ and rescattered $b_1(\mathbf{p},t_F)$ transition amplitudes, i.e.,

$$\begin{aligned}|b(\mathbf{p},t_F)|^2 &= |b_0(\mathbf{p},t_F)+b_1(\mathbf{p},t_F)|^2,\\ &= |b_0(\mathbf{p},t_F)|^2+|b_1(\mathbf{p},t_F)|^2\\ &\quad + b_0(\mathbf{p},t_F)b_1^*(\mathbf{p},t_F)+\text{c.c.}\end{aligned} \tag{9}$$

III. TRANSITION MATRIX AMPLITUDES CALCULATION

We aim to employ two different models to calculate the total photoelectron spectra of molecular systems, namely, (i) model A, in which we employ a separable nonlocal SR potential to calculate both the bound and scattering states, as well as the bound-free and continuum-continuum matrix element, and (ii) model B, in which the initial ground state is modeled as an LCAO and a nonlocal SR potential is used to compute the scattering states and the continuum-continuum matrix element. The bound-free transition matrix element is then obtained employing an LCAO for the bound part and a nonlocal SR potential scattering state for the continuum part.

A. Bound states and dipole transition matrix element: Nonlocal SR potential

To obtain the bound and rescattering states we propose to use a separable nonlocal SR potential as

$$V(\mathbf{p},\mathbf{p}') = \frac{-\gamma'}{\sqrt{(p^2+\Gamma^2)(p'^2+\Gamma^2)}}\sum_{j=1}^{3} e^{-i\mathbf{R}_j\cdot(\mathbf{p}-\mathbf{p}')}. \tag{10}$$

This potential describes the interaction between the active electron and each of the nuclei of the molecule, and depends on the their positions $\mathbf{R}_j$. The parameters γ' and Γ are constants related with the shape of the ground state (for a more detailed description see [29–31,38]).

The stationary Schrödinger equation for the molecule in absence of the laser field in momentum representation reads as follows:

$$\frac{p^2}{2}\Psi_{0_{SR}}(\mathbf{p}) - \frac{\gamma'}{\sqrt{p^2+\Gamma^2}}\sum_{j=1}^{3} e^{-i\mathbf{R}_j\cdot\mathbf{p}}\breve{\varphi}_j = E_0\Psi_{0_{SR}}(\mathbf{p}), \tag{11}$$

where E_0 denotes the energy of the bound state and $E_0 = -I_p$. Defining a new set of variables $\breve{\varphi}_j = \int \frac{d^3\mathbf{p}'\Psi_{0_{SR}}(\mathbf{p}')e^{i\mathbf{R}_j\cdot\mathbf{p}'}}{\sqrt{p'^2+\Gamma^2}}$ we obtain the bound states that can explicitly be written as

$$\Psi_{0_{SR}}(\mathbf{p}) = \frac{\gamma'\left(\breve{\varphi}_1 e^{-i\mathbf{R}_1\cdot\mathbf{p}} + \breve{\varphi}_2 e^{-i\mathbf{R}_2\cdot\mathbf{p}} + \breve{\varphi}_3 e^{-i\mathbf{R}_3\cdot\mathbf{p}}\right)}{\sqrt{p^2+\Gamma^2}\left(\frac{p^2}{2}+I_p\right)}. \tag{12}$$

The exact values of the variables $\breve{\varphi}_j$ are determined by solving an eigenvalues problem (see [29,31] for more details) where $\breve{\varphi}_1 = \breve{\varphi}_3 = (\frac{I_2}{I_1-I_3})\breve{\varphi}_2$.

Once we obtain the bound states, the dipole transition matrix element $\mathbf{d}_{SR}(\mathbf{p}_0)$ can then be computed as

$$\begin{aligned}\mathbf{d}_{SR}(\mathbf{p}_0) &= \sum_{j=1}^{3}\mathbf{d}_{SR_j}(\mathbf{p}_0) = -2i\,\mathcal{M}\mathcal{A}(\mathbf{p}_0)\\ &\quad\times\left[\frac{I_2}{I_1-I_3}\left(e^{-i\mathbf{R}_1\cdot\mathbf{p}_0}+e^{-i\mathbf{R}_3\cdot\mathbf{p}_0}\right)+1\right],\end{aligned} \tag{13}$$

where $\mathcal{M}$ is a normalization constant and $\mathcal{A}(\mathbf{p}_0)$, I_1, I_2, and I_3 are the same as those defined in [31]. Similarly, we can write the dipole transition matrix for the two-center system (see the Appendix for more details), defined as a sum over each of the two atoms placed at $\mathbf{R}_j$, with $j = 1,2$ [29].

B. Scattering waves and the continuum-continuum transition matrix element

To obtain the scattering states we follow the same procedure as in the previous sub-section. Let us consider a scattering wave $\Psi_{\mathbf{p}_0}(\mathbf{p})$, with asymptotic momentum $\mathbf{p}_0$, as a coherent superposition of a plane wave and an extra correction:

$$\Psi_{\mathbf{p}_0}(\mathbf{p}) = \delta(\mathbf{p}-\mathbf{p}_0) + \sum_{j=1}^{3}\delta\Psi_{\mathbf{R}_j\mathbf{p}_0}(\mathbf{p}). \tag{14}$$

This state has an energy $E = \mathbf{p}_0^2/2$. Moreover, after some algebra and substituting the nonlocal SR potential, the correction then results in the following:

$$\delta\Psi_{\mathbf{R}_j\mathbf{p}_0}(\mathbf{p}) = \frac{-2\gamma'\,e^{-i\mathbf{R}_j\cdot\mathbf{p}}}{\sqrt{p^2+\Gamma^2}\left(p_0^2-p^2+i\epsilon\right)}\left[\frac{e^{i\mathbf{R}_j\cdot\mathbf{p}_0}}{\sqrt{p_0^2+\Gamma^2}}+\breve{\varphi}'_j\right], \tag{15}$$

where the variables are defined by $\breve{\varphi}'_j = \int \frac{d^3\mathbf{p}'e^{i\mathbf{R}_j\cdot\mathbf{p}'}\,\delta\Psi_{\mathbf{p}_0}(\mathbf{p}')}{\sqrt{p'^2+\Gamma^2}}$. Notice that ϵ is another infinitesimal parameter to avoid the divergence at the "energy shell," $p^2 = p_0^2$. This singularity is avoided due to the finite spread of the involved wave packets. In the numerical calculations we smooth this singularity, allowing ϵ to be of the order of 1 (see [29,30] for more details).

To obtain the explicit form of $\breve{\varphi}'_j$ we need to solve an eigenvalues problem for the scattering states (similar to the procedure employed with the bound states). For our three-center molecular system the total scattering wave function can also be written as a composition of three functions, each centered at $\mathbf{R}_1$, $\mathbf{R}_2$, and $\mathbf{R}_3$. Explicitly, we then have

$$\delta\Psi_{\mathbf{R}_1\mathbf{p}_0}(\mathbf{p}) = \frac{-\mathcal{D}_{11}(\mathbf{p}_0)\,e^{-i\mathbf{R}_1\cdot(\mathbf{p}-\mathbf{p}_0)} - \mathcal{D}_{12}(\mathbf{p}_0)\,e^{-i\mathbf{R}_1\cdot\mathbf{p}+i\mathbf{R}_2\cdot\mathbf{p}_0} - \mathcal{D}_{13}(\mathbf{p}_0)\,e^{-i\mathbf{R}_1\cdot\mathbf{p}+i\mathbf{R}_3\cdot\mathbf{p}_0}}{\sqrt{p^2+\Gamma^2}\left(p_0^2-p^2+i\epsilon\right)}, \tag{16}$$

$$\delta\Psi_{\mathbf{R}_2\mathbf{p}_0}(\mathbf{p}) = \frac{-\mathcal{D}_0(\mathbf{p}_0)\,e^{-i\mathbf{R}_2\cdot(\mathbf{p}-\mathbf{p}_0)} - \mathcal{D}_{12}(\mathbf{p}_0)\,e^{-i\mathbf{R}_2\cdot\mathbf{p}+i\mathbf{R}_1\cdot\mathbf{p}_0} - \mathcal{D}_{12}(\mathbf{p}_0)\,e^{-i\mathbf{R}_2\cdot\mathbf{p}+i\mathbf{R}_3\cdot\mathbf{p}_0}}{\sqrt{p^2+\Gamma^2}\left(p_0^2-p^2+i\epsilon\right)}, \tag{17}$$

and

$$\delta\Psi_{\mathbf{R}_3\mathbf{p}_0}(\mathbf{p}) = \frac{-\mathcal{D}_{11}(\mathbf{p}_0)\, e^{-i\mathbf{R}_3\cdot(\mathbf{p}-\mathbf{p}_0)} - \mathcal{D}_{12}(\mathbf{p}_0)\, e^{-i\mathbf{R}_3\cdot\mathbf{p}+i\mathbf{R}_2\cdot\mathbf{p}_0} - \mathcal{D}_{13}(\mathbf{p}_0)\, e^{-i\mathbf{R}_3\cdot\mathbf{p}+i\mathbf{R}_1\cdot\mathbf{p}_0}}{\sqrt{p^2+\Gamma^2}\left(p_0^2-p^2+i\epsilon\right)}. \tag{18}$$

In here the total correction to the scattering state is $\delta\Psi_{\mathbf{p}_0}(\mathbf{p}) = \mathcal{M}_{\rm scat}\sum_{j=1}^{3}\delta\Psi_{\mathbf{R}_j\mathbf{p}_0}(\mathbf{p})$, where $\mathcal{M}_{\rm scat} = \frac{1}{(1+I'_{11})^2+(1+I'_{11})I'_{13}-2{I'_{12}}^2}$ is a normalization constant. The integration "constants" for the scattering states in Eqs. (16)–(18) have the following functional form:

$$\mathcal{D}_{11}(\mathbf{p}_0) = \frac{2\gamma'}{\sqrt{p_0^2+\Gamma^2}}\left[\frac{(1+I'_{11})^2-{I'_{12}}^2}{1+I'_{11}-I'_{13}}\right], \tag{19}$$

$$\mathcal{D}_{0}(\mathbf{p}_0) = \frac{2\gamma'}{\sqrt{p_0^2+\Gamma^2}}[1+I'_{11}+I'_{13}], \tag{20}$$

$$\mathcal{D}_{12}(\mathbf{p}_0) = \frac{2\gamma'}{\sqrt{p_0^2+\Gamma^2}}[-I'_{12}], \tag{21}$$

and

$$\mathcal{D}_{13}(\mathbf{p}_0) = \frac{2\gamma'}{\sqrt{p_0^2+\Gamma^2}}\left[\frac{{I'_{12}}^2-I'_{13}(1+I'_{11})}{1+I'_{11}-I'_{13}}\right], \tag{22}$$

where

$$I'_{jj'} = -2\gamma'\int d^3\mathbf{p}\,\frac{e^{i(\mathbf{R}_j-\mathbf{R}_{j'})\cdot\mathbf{p}}}{(p^2+\Gamma^2)\left(p_0^2-p^2+i\epsilon\right)}. \tag{23}$$

The case of diatomics can be obtained from $\Psi_{2-\mathbf{p}_0} = \delta(\mathbf{p}-\mathbf{p}_0)+\sum_{j=1}^{2}\delta\Psi_{2-\mathbf{R}_j\mathbf{p}_0}(\mathbf{p})$ (see the Appendix and [29] for more details).

Once the rescattering states are completely defined we proceed to the evaluation of the continuum-continuum transition matrix element using Eq. (4). We thus have

$$\mathbf{g}(\mathbf{p}_1,\mathbf{p}_2) = \mathcal{M}_{\rm scat}\sum_{j=1}^{3}[i\nabla_{\mathbf{p}}\delta\Psi_{\mathbf{R}_j\mathbf{p}_2}(\mathbf{p}) - \mathbf{R}_j\delta\Psi_{\mathbf{R}_j\mathbf{p}_2}(\mathbf{p})]|_{\mathbf{p}_1} + \mathcal{M}_{\rm scat}\sum_{j=1}^{3}[i\nabla_{\mathbf{p}}\delta\Psi_{\mathbf{R}_j\mathbf{p}_1}(\mathbf{p}) - \mathbf{R}_j\delta\Psi_{\mathbf{R}_j\mathbf{p}_1}(\mathbf{p})]^*|_{\mathbf{p}_2}. \tag{24}$$

For our three-center molecular system we get an independent transition matrix element for each of the possible rescattering scenarios, i.e.,

$$\begin{aligned}
\mathbf{g}_{11}(\mathbf{p}_1,\mathbf{p}_2) &= \mathcal{Q}_{11}(\mathbf{p}_1,\mathbf{p}_2)\, e^{-i\mathbf{R}_1\cdot(\mathbf{p}_1-\mathbf{p}_2)},\\
\mathbf{g}_{22}(\mathbf{p}_1,\mathbf{p}_2) &= \mathcal{Q}_{0}(\mathbf{p}_1,\mathbf{p}_2)\, e^{-i\mathbf{R}_2\cdot(\mathbf{p}_1-\mathbf{p}_2)},\\
\mathbf{g}_{33}(\mathbf{p}_1,\mathbf{p}_2) &= \mathcal{Q}_{11}(\mathbf{p}_1,\mathbf{p}_2)\, e^{-i\mathbf{R}_3\cdot(\mathbf{p}_1-\mathbf{p}_2)},\\
\mathbf{g}_{12}(\mathbf{p}_1,\mathbf{p}_2) &= \mathcal{Q}_{12}(\mathbf{p}_1,\mathbf{p}_2)\, e^{-i\mathbf{R}_2\cdot\mathbf{p}_1+i\mathbf{R}_1\cdot\mathbf{p}_2},\\
\mathbf{g}_{21}(\mathbf{p}_1,\mathbf{p}_2) &= \mathcal{Q}_{12}(\mathbf{p}_1,\mathbf{p}_2)\, e^{-i\mathbf{R}_1\cdot\mathbf{p}_1+i\mathbf{R}_2\cdot\mathbf{p}_2},\\
\mathbf{g}_{13}(\mathbf{p}_1,\mathbf{p}_2) &= \mathcal{Q}_{13}(\mathbf{p}_1,\mathbf{p}_2)\, e^{-i\mathbf{R}_3\cdot\mathbf{p}_1+i\mathbf{R}_1\cdot\mathbf{p}_2},\\
\mathbf{g}_{31}(\mathbf{p}_1,\mathbf{p}_2) &= \mathcal{Q}_{13}(\mathbf{p}_1,\mathbf{p}_2)\, e^{-i\mathbf{R}_1\cdot\mathbf{p}_1+i\mathbf{R}_3\cdot\mathbf{p}_2},\\
\mathbf{g}_{23}(\mathbf{p}_1,\mathbf{p}_2) &= \mathcal{Q}_{12}(\mathbf{p}_1,\mathbf{p}_2)\, e^{-i\mathbf{R}_3\cdot\mathbf{p}_1+i\mathbf{R}_2\cdot\mathbf{p}_2},\\
\mathbf{g}_{32}(\mathbf{p}_1,\mathbf{p}_2) &= \mathcal{Q}_{12}(\mathbf{p}_1,\mathbf{p}_2)\, e^{-i\mathbf{R}_2\cdot\mathbf{p}_1+i\mathbf{R}_3\cdot\mathbf{p}_2},
\end{aligned} \tag{25}$$

where the $\mathcal{Q}_{jj'}$, are defined by

$$\mathcal{Q}_{11}(\mathbf{p}_1,\mathbf{p}_2) = -i\mathcal{M}_{\rm scat}\,[\mathcal{D}(\mathbf{p}_2)\mathcal{C}_1(\mathbf{p}_1,\mathbf{p}_2) - \mathcal{D}^*(\mathbf{p}_1)\mathcal{C}_2(\mathbf{p}_1,\mathbf{p}_2)], \tag{26}$$

$$\mathcal{Q}_{0}(\mathbf{p}_1,\mathbf{p}_2) = -i\mathcal{M}_{\rm scat}\,[\mathcal{D}_0(\mathbf{p}_2)\mathcal{C}_1(\mathbf{p}_1,\mathbf{p}_2) - \mathcal{D}_0^*(\mathbf{p}_1)\mathcal{C}_2(\mathbf{p}_1,\mathbf{p}_2)], \tag{27}$$

$$\mathcal{Q}_{12}(\mathbf{p}_1,\mathbf{p}_2) = -i\mathcal{M}_{\rm scat}\,[\mathcal{D}_{12}(\mathbf{p}_2)\mathcal{C}_1(\mathbf{p}_1,\mathbf{p}_2) - \mathcal{D}_{12}^*(\mathbf{p}_1)\mathcal{C}_2(\mathbf{p}_1,\mathbf{p}_2)], \tag{28}$$

$$\mathcal{Q}_{13}(\mathbf{p}_1,\mathbf{p}_2) = -i\mathcal{M}_{\rm scat}\,[\mathcal{D}_{13}(\mathbf{p}_2)\mathcal{C}_1(\mathbf{p}_1,\mathbf{p}_2) - \mathcal{D}_{13}^*(\mathbf{p}_1)\mathcal{C}_2(\mathbf{p}_1,\mathbf{p}_2)], \tag{29}$$

and

$$\begin{aligned}
\mathcal{C}_1(\mathbf{p}_1,\mathbf{p}_2) &= \left[\frac{\mathbf{p}_1\left(3p_1^2-p_2^2+2\Gamma^2\right)}{\left(p_1^2+\Gamma^2\right)^{\frac{3}{2}}\left(p_2^2-p_1^2+i\epsilon\right)^2}\right],\\
\mathcal{C}_2(\mathbf{p}_1,\mathbf{p}_2) &= \left[\frac{\mathbf{p}_2\left(3p_2^2-p_1^2+2\Gamma^2\right)}{\left(p_2^2+\Gamma^2\right)^{\frac{3}{2}}\left(p_1^2-p_2^2-i\epsilon\right)^2}\right].
\end{aligned} \tag{30}$$

All the equations obtained in this subsection are consistent with the atomic and diatomic cases presented in previous publications (see [29,30]). In fact, all the cases are identical when the internuclear distance goes to zero, $\mathbf{R}\to 0$. The verification of this limit for the direct processes is straightforward. Here, the phase factor becomes the well-known semiclassical action $S(\mathbf{p},t,t')$ and the transition amplitude exactly has the same dependency as for an atom, if we replace the atomic matrix elements on it. For the rescattering events, on the other hand, we have to neglect the contribution of the nonlocal and cross terms ($j\neq j'$) in Eq. (8) and follow the same procedure as in the case of the direct processes. In the following sections we obtain the exact dependency of the rescattered matrix elements that also describe the atomic case when $\mathbf{R}\to 0$.

C. Bound states and the dipole transition matrix element: The molecular orbital as a LCAO

In this section we are going to calculate the molecular bound states as a LCAO of Gaussian-like functions. Our formulation takes full advantage of the GAMESS package [39,40]. For simplicity we use a STO-3G basis set, but note that our approach is quite general and other basis sets could be employed.

Let us define the bound state of the molecular system as

$$\Psi_{0_{\rm LCAO}}(\mathbf{p}) = \sum_{j=1}^{3}\sum_{i=1}^{5} G_{j(i)}\Phi_{j(i)}(\mathbf{p}), \tag{31}$$

where the index j represents the number of the atoms in the molecule. Furthermore, the index i accounts for the different atomic orbitals (AOs). Throughout our paper we model molecular systems using only $i = 1 \to 1s, 2 \to 2s$, and $3,4,5 \to 2p_{x,y,z}$ states, but states with other quantum numbers could be implemented.

Furthermore, $G_{j(i)}$ is a constant defining the *weight* of each atom orbital. In our case we consider the HOMO and the particular values are obtained using GAMESS. Finally, the functions $\Phi_{j(i)}(\mathbf{p})$ define the atomic orbitals. For instance, an atomic orbital based on s states can be written as

$$\Phi_{j(s)}(\mathbf{p}) = e^{-i\mathbf{R}_j\cdot\mathbf{p}}\,\frac{1}{2^{3/2}}\sum_{n=1}^{3}\frac{C_{n;j(s)}}{\zeta_{n;j(s)}^{3/2}}\,e^{\frac{-\mathbf{p}^2}{4\zeta_{n;j(s)}}}, \tag{32}$$

while one for $2p$ states can be written as

$$\Phi_{j(2p_r)}(\mathbf{p}) = -i\;p_r\;e^{-i\mathbf{R}_j\cdot\mathbf{p}}\,\frac{1}{2^{5/2}}\sum_{n=1}^{3}\frac{C_{n;j(p_r)}}{\zeta_{n;j(p_r)}^{5/2}}\,e^{\frac{-\mathbf{p}^2}{4\zeta_{n;j(p_r)}}}. \tag{33}$$

Here the index r can take the value x, y, or z. The coefficients $C_{n;j(s,p_r)}$ and $\zeta_{n;j(s,p_r)}$ are obtained using, for example, a Roothaan-Hartree-Fock optimization scheme (see [39,40] for more details).

The dipole transition matrix element within this model, that describes the transition of the electron from the bound to the continuum state, then reads as

$$\begin{aligned}\mathbf{d}_{\mathrm{LCAO}}(\mathbf{p}_0) = -\sum_{j=1}^{3}\sum_{i=1}^{5} G_{j(i)}\{i\nabla_{\mathbf{p}}\,\Phi_{j(i)}(\mathbf{p})|_{\mathbf{p}_0} \\ -\mathbf{R}_j\,\Phi_{j(i)}(\mathbf{p}_0)\},\end{aligned} \tag{34}$$

where depending on the states' character the gradient results in

$$i\nabla_{\mathbf{p}}\,\Phi_{j(1s)}(\mathbf{p})|_{\mathbf{p}_0} = \mathbf{R}_j\,\Phi_{j(1s)}(\mathbf{p}_0) - \frac{i\,\mathbf{p}_0}{2\,\zeta_{n;j(s)}}\,\Phi_{j(1s)}(\mathbf{p}_0) \tag{35}$$

for the s states and

$$\begin{aligned}i\nabla_{\mathbf{p}}\,\Phi_{j(2p_r)}(\mathbf{p})|_{\mathbf{p}_0} = \mathbf{R}_j\,\Phi_{j(2p_r)}(\mathbf{p}_0) - \frac{i\,\mathbf{p}_0\Phi_{j(2p_r)}(\mathbf{p}_0)}{2\,\zeta_{n;j(2p_r)}} \\ +\delta\Phi_{j(2p_r)}(\mathbf{p}_0)\,\hat{\mathbf{r}},\end{aligned} \tag{36}$$

where

$$\delta\Phi_{j(2p_r)}(\mathbf{p}_0) = e^{-i\mathbf{R}_j\cdot\mathbf{p}_0}\,\frac{1}{2^{5/2}}\sum_{n=1}^{3}\frac{C_{n;j(2p_z)}}{\zeta_{n;j(2p_z)}^{5/2}}\,e^{\frac{-\mathbf{p}_0^2}{4\zeta_{n;j(2p_z)}}}, \tag{37}$$

for the p states.

Using the above equations we are able to obtain analytical expressions for the molecular dipole transition matrix elements. As was noted in this section, we introduced the formulation particularized for three-center molecular systems. Nevertheless, and for completeness, we present in the next subsections expressions for two prototypical two-center molecules, O_2 and CO, as well. Additionally, our three-center examples will be based on the CO_2 and CS_2 molecules.

1. O_2

The bound state (HOMO) for the O_2 molecule oriented on the y axis, written as a LCAO, reads as

$$\Psi_{0-\mathrm{O}_2}(\mathbf{p}) = G_{1(2p_z)}\Phi_{1(2p_z)}(\mathbf{p}) + G_{2(2p_z)}\Phi_{2(2p_z)}(\mathbf{p}). \tag{38}$$

The inset of Fig. 3(b) illustrates what Eq. (38) looks like in position space. Furthermore, the dipole transition matrix element can be computed from

$$\begin{aligned}\mathbf{d}_{\mathrm{O}_2}(\mathbf{p}_0) = -\sum_{j=1}^{2} G_{j(2p_z)}\,\{i\nabla_{\mathbf{p}}\,\Phi_{j(2p_z)}(\mathbf{p})|_{\mathbf{p}_0} \\ -\mathbf{R}_j\,\Phi_{j(2p_z)}(\mathbf{p}_0)\},\end{aligned} \tag{39}$$

where explicitly we then have

$$\begin{aligned}\mathbf{d}_{\mathrm{O}_2}(\mathbf{p}_0) = \; G_{1(2p_z)}\left\{i\,\mathbf{p}_0\frac{\Phi_{1(2p_z)}(\mathbf{p}_0)}{2\,\zeta_{n;1(2p_z)}} - \delta\Phi_{1(2p_z)}(\mathbf{p}_0)\,\hat{\mathbf{k}}\right\} \\ + G_{2(2p_z)}\left\{i\,\mathbf{p}_0\frac{\Phi_{2(2p_z)}(\mathbf{p}_0)}{2\,\zeta_{n;2(2p_z)}} - \delta\Phi_{2(2p_z)}(\mathbf{p}_0)\,\hat{\mathbf{k}}\right\}.\end{aligned} \tag{40}$$

The parameters $G_{(1,2)(2p_z)}$ and $\zeta_{n;1/2(2p_z)}$ are obtained setting the molecule in its equilibrium position via an optimization procedure using GAMESS [39,40].

2. CO

For the case of the CO molecule the bound state is a composition of $1s$, $2s$, and $2p$ states described by

$$\begin{aligned}\Psi_{0-\mathrm{CO}}(\mathbf{p}) = \sum_{j=1}^{2}[G_{j(1s)}\Phi_{j(1s)}(\mathbf{p}) + G_{j(2s)}\Phi_{j(2s)}(\mathbf{p}) \\ + G_{j(2p_z)}\Phi_{j(2p_z)}(\mathbf{p})].\end{aligned} \tag{41}$$

The dipole transition matrix element reads as

$$\begin{aligned}\mathbf{d}_{\mathrm{CO}}(\mathbf{p}_0) = \sum_{j=1}^{2}\Bigg[G_{j(1s)}\left\{i\,\mathbf{p}_0\frac{\Phi_{j(1s)}(\mathbf{p}_0)}{2\,\zeta_{n;j(1s)}}\right\} \\ + G_{j(2s)}\left\{i\,\mathbf{p}_0\frac{\Phi_{j(2s)}(\mathbf{p}_0)}{2\,\zeta_{n;j(2s)}}\right\} \\ + G_{j(2p_z)}\left\{i\,\mathbf{p}_0\frac{\Phi_{j(2p_z)}(\mathbf{p}_0)}{2\,\zeta_{n;j(2p_z)}} - \delta\Phi_{j(2p_z)}(\mathbf{p}_0)\,\hat{\mathbf{k}}\right\}\Bigg].\end{aligned} \tag{42}$$

3. CO_2

For the case of CO_2 the bound state is

$$\Psi_{0-\mathrm{CO}_2}(\mathbf{p}) = \sum_{j=1}^{3}[G_{j(2p_x)}\Phi_{j(2p_x)}(\mathbf{p}) + G_{j(2p_z)}\Phi_{j(2p_z)}(\mathbf{p})]. \tag{43}$$

A plot of the HOMO for this molecule, using Eq. (43), is shown in Fig. 2(a), where we consider the molecule in equilibrium—each of the C-O bond lengths is set to 2.2 a.u. (1.164 Å), and oriented perpendicular to the laser field (linearly polarized along the z axis).

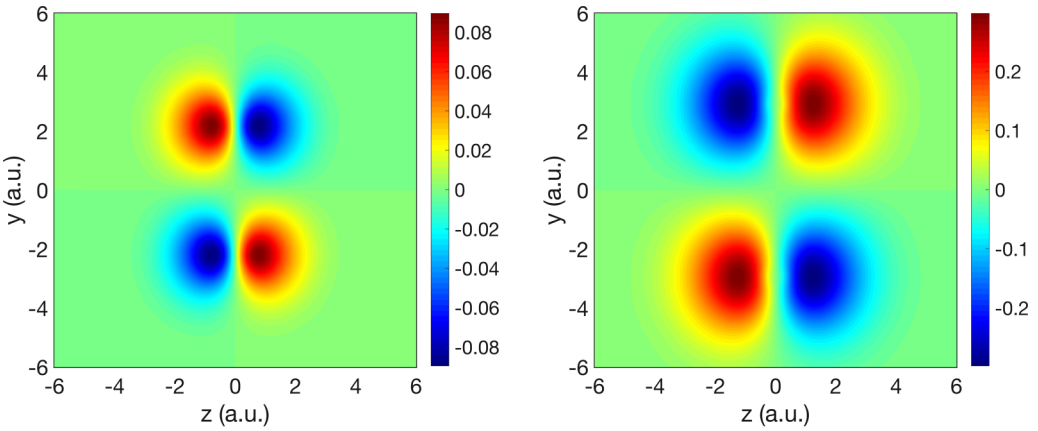

(a) (b)

FIG. 2. Sectional view of the constructed HOMO, presented in the z-y plane, calculated using the LCAO method, $\Psi_{0_{\mathrm{LCAO}}}(\mathbf{r})$. (a) CO_2 and (b) CS_2 (see the text for details).

The dipole transition matrix element can be explicitly written as

$$\mathbf{d}_{\mathrm{CO_2}}(\mathbf{p}_0) = \sum_{j=1}^{3}\Bigg[G_{j(2p_x)}\left\{i\,\mathbf{p}_0\frac{\Phi_{j(2p_x)}(\mathbf{p}_0)}{2\,\zeta_{n;j(2p_x)}} - \delta\Phi_{j(2p_x)}(\mathbf{p}_0)\,\hat{\mathbf{i}}\right\} + G_{j(2p_z)}\left\{i\,\mathbf{p}_0\frac{\Phi_{j(2p_z)}(\mathbf{p}_0)}{2\,\zeta_{n;j(2p_z)}} - \delta\Phi_{j(2p_z)}(\mathbf{p}_0)\,\hat{\mathbf{k}}\right\}\Bigg]. \tag{44}$$

4. CS_2

The CS_2 bound state within the LCAO approach reads as

$$\Psi_{0-\mathrm{CS_2}}(\mathbf{p}) = \sum_{j=1}^{3}[G_{j(2p_x)}\Phi_{j(2p_x)}(\mathbf{p}) + G_{j(2p_z)}\Phi_{j(2p_z)}(\mathbf{p}) + G_{j(3p_x)}\Phi_{j(3p_x)}(\mathbf{p}) + G_{j(3p_z)}\Phi_{j(3p_z)}(\mathbf{p})]. \tag{45}$$

As in the previous case, we consider the CS_2 molecule in equilibrium—each of the C-S bond lengths is set to 2.92 a.u.(1.545 Å), and oriented perpendicular to the laser field (polarized along the z axis). A plot of the CS_2 HOMO is depicted in Fig. 2(b).

Finally, the dipole transition matrix element for the CS_2 molecule reads as

$$\mathbf{d}_{\mathrm{CS_2}}(\mathbf{p}_0) = \sum_{j=1}^{3}\Bigg[G_{j(2p_x)}\left\{i\,\mathbf{p}_0\frac{\Phi_{j(2p_x)}(\mathbf{p}_0)}{2\,\zeta_{j;n(2p_x)}} - \delta\Phi_{j(2p_x)}(\mathbf{p}_0)\,\hat{\mathbf{i}}\right\} + G_{j(2p_z)}\left\{i\,\mathbf{p}_0\frac{\Phi_{j(2p_z)}(\mathbf{p}_0)}{2\,\zeta_{j;n(2p_z)}} - \delta\Phi_{j(2p_z)}(\mathbf{p}_0)\,\hat{\mathbf{k}}\right\} + G_{j(3p_x)}\left\{i\,\mathbf{p}_0\frac{\Phi_{j(3p_x)}(\mathbf{p}_0)}{2\,\zeta_{j;n(3p_x)}} - \delta\Phi_{j(3p_x)}(\mathbf{p}_0)\,\hat{\mathbf{i}}\right\} + G_{j(3p_z)}\left\{i\,\mathbf{p}_0\frac{\Phi_{j(3p_z)}(\mathbf{p}_0)}{2\,\zeta_{j;n(3p_z)}} - \delta\Phi_{j(3p_z)}(\mathbf{p}_0)\,\hat{\mathbf{k}}\right\}\Bigg]. \tag{46}$$

After obtaining both the dipole and the continuum-continuum transition matrix elements it is then possible to

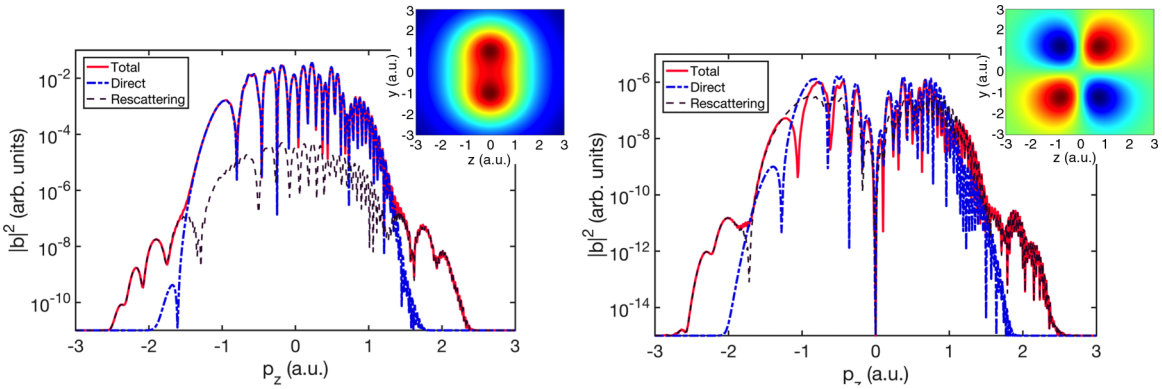

(a) (b)

FIG. 3. (a) Total, direct, and rescattering contributions to the photoelectron spectra as a function of the final momentum. The HOMO of the molecule is computed using the SR potential. (b) The same as in panel (a) but now the HOMO is modeled using a LCAO. The HOMOs for both cases are shown as insets. In all the cases, we used an O_2 molecule oriented perpendicular to the laser field polarization (see text for more details).

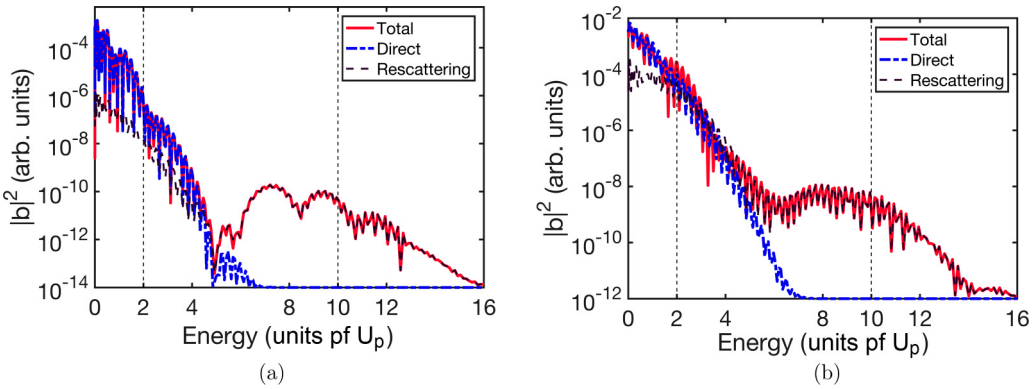

FIG. 4. Total, direct, and rescattering contributions to the photoelectron spectra, as a function of the electron energy in U_p units, for the CO molecule. (a) Model A. (b) Model B. We consider the CO molecule is in equilibrium, the internuclear distance is set to $R = 2.13$ a.u. (1.127 Å), and the molecule is oriented parallel to the laser field polarization (see text for more details).

compute Eqs. (5), (8), and (9) to obtain the direct, the rescattering, and the total photoelectron transition amplitudes. We stress that our model only involves, in the worst case scenario, the numerical calculation of a 2D integral, the rest of the expressions being written in terms of fully analytical functions.

IV. RESULTS AND DISCUSSION

In this section, we compute the ATI spectra generated from different molecular systems using two different approaches, namely, models A and B as described in Sec. III. We compare the ATI spectra for four different molecular systems in order to establish similarities and differences. Furthermore, the splitting of the contributions to the photoelectron spectra helps us to distinguish which of the direct and rescattering scenarios is relevant in the different energy and momentum regions.

In all the simulations we use an ultrashort laser pulse with a central frequency $\omega_0 = 0.057$ a.u. (wavelength $\lambda = 800$ nm), a $\sin^2$ envelope shape, and $N_c = 4$ total cycles (this corresponds to a full width at half maximum of 5.2 fs). The carrier-envelope phase (CEP) is set to $\phi_0 = 0$ rad and the time step is set to $\delta t = 0.02$ a.u. The numerical integration time window is then t: $[0, t_F]$, where $t_F = N_c T_0 \approx 11$ fs and $T_0 = 2\pi/\omega_0$ denote the final "detection" time and the cycle period of the laser field, respectively.

A. Results on diatomic molecules: O_2 and CO

In this section, we apply our analytical model using the equations presented in the Appendix to calculate the photoelectron spectra of two prototypical diatomic systems: O_2 and CO. The numerical integration of the photoelectron spectra by means of Eqs. (5) and (8) has been performed via a rectangular rule with particular emphasis on the convergence of the results. As the final momentum distribution, Eq. (9), is "locally" independent of the momentum $\mathbf{p}$, $|b(\mathbf{p},t)|^2$ can be computed concurrently for a given set of $\mathbf{p}$ values. We have optimized the calculation of the whole transition amplitude, $|b(\mathbf{p},t)|^2$, by using the OpenMP parallel package [41]. The final momentum photoelectron distribution, $|b(\mathbf{p},t)|^2$, is computed in a 1D-momentum line along p_z and a 2D-momentum p_z-p_y plane.

1. O_2 *molecule*

The computation of the photoelectron spectra was performed by using Eqs. (9), (A3), and (A8) for the case of model A. Here we set $\Gamma = 1$ and $\gamma = 0.08$ a.u. in our nonlocal SR potential in order to match the dioxygen ionization potential obtained with GAMESS, $I_p = 0.334$ a.u for the singlet state. Next, in the case of the calculation using model B, we use Eqs. (9), (40), and (A8).

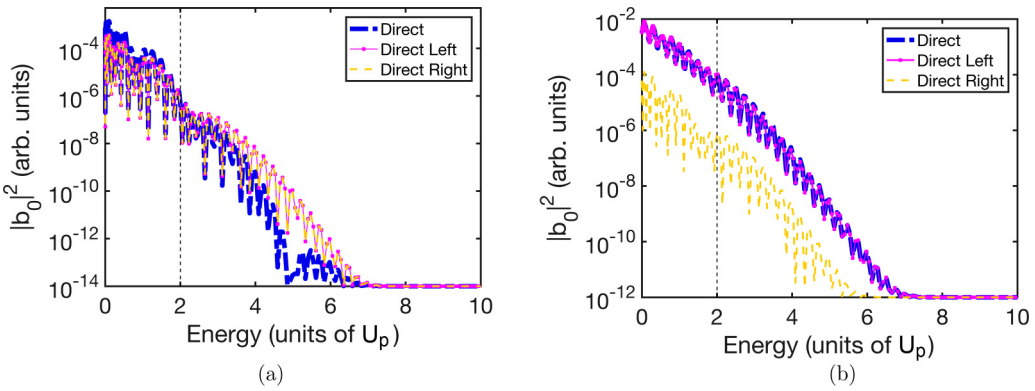

FIG. 5. Direct contributions to the CO photoelectron spectra (in logarithmic scale) as a function of the electron energy, in U_p units, calculated by using (a) model A and (b) model B. We consider the CO molecule is in equilibrium, the internuclear distance is set to $R = 2.13$ a.u. (1.127 Å), and the molecule is oriented parallel, aligned at 0° with respect to the laser field polarization (see text for more details).

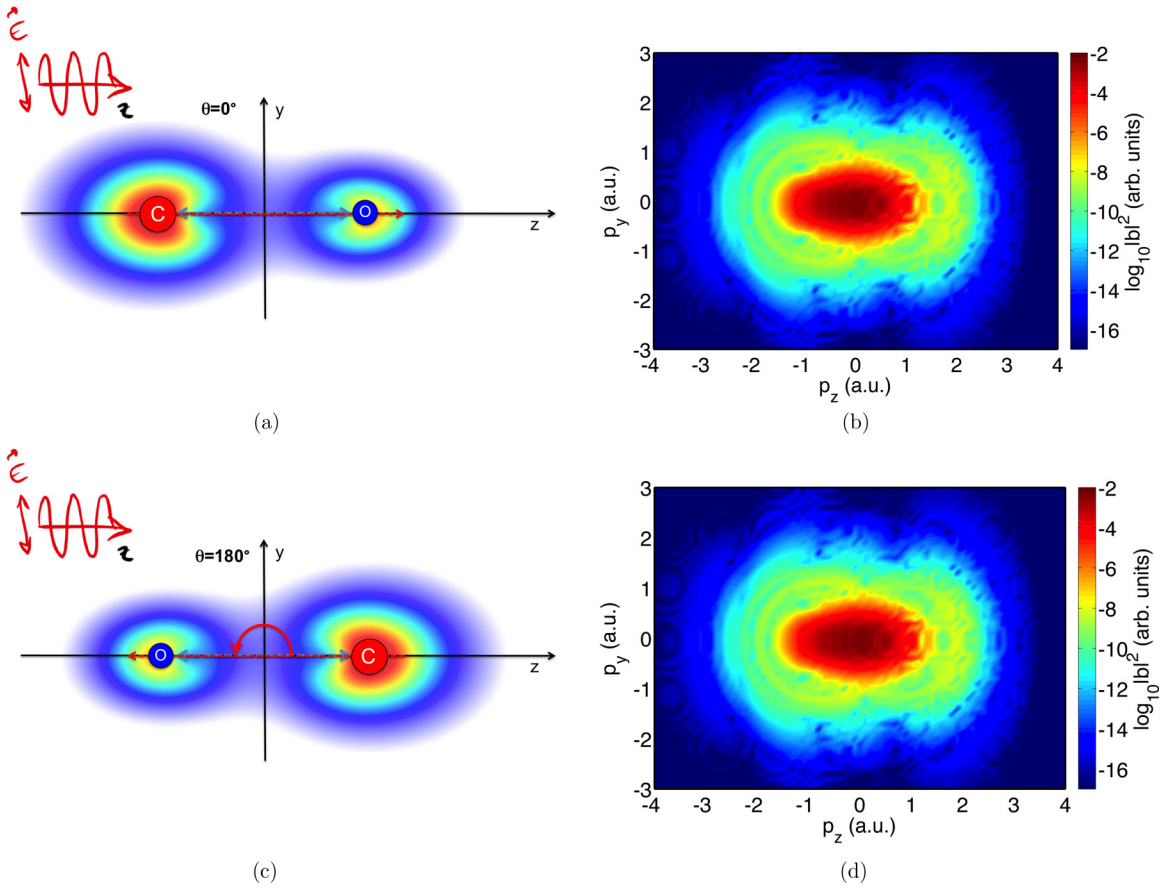

FIG. 6. (a) Representation of the CO molecule aligned at 0° with respect to the laser field polarization. (b) Total ATI photoelectron spectra (in logarithmic scale) for a 2D-momentum plane (p_z, p_y). (c, d) The same as in panels (a, b) but for the molecule aligned at 180° with the laser field polarization.

In Fig. 3(a) we present the results using model A. Here, we use the nonlocal SR potential to obtain the ground state and the bound-free dipole matrix element. This kind of potential only supports s states as we can see in the inset of Fig. 3(a). In contrast, model B gives a more accurate description of the O_2 molecular orbital (MO) [see inset Fig. 3(b)].

The shape of the MO introduces noticeable differences in the different contributions of the photoelectron spectra. Figures 3(a) and 3(b) show the main contributions to the full final photoelectron spectra, namely, the total $|b(\mathbf{p},t)|^2$ (red solid line), the direct $|b_0(\mathbf{p},t)|^2$ (dashed with points blue line), and the rescattering $|b_1(\mathbf{p},t)|^2$ (black dashed line) terms [see Eq. (9)]. The black solid lines define the two cutoffs defined by $2U_p$ and $10U_p$. As we can infer from the latter figures the two models show slightly different behaviors. In the case of model A, that describes the HOMO as a superposition of two one-electron $1s$ AOs, Fig. 3(a), we see an overestimation of the direct processes. This fact could be caused by the kind of SR potential used to get the molecular ground state. This SR potential does not properly describe the attraction force felt by the electron both when it is bound and in the continuum. In this way this electron could "escape" more easily from the ionic core and becomes a "direct electron."

Results from the two models also show some similarities: stronger oscillations for small values of the electron momentum followed by a rapid decrease of the ATI yield (at $|p_z| \lesssim 1.0$ a.u.), a plateau where the amplitude remains almost constant, and the fact that both approaches end up with an abrupt cutoff around the same value of $|p_z| \lesssim 2.1$ a.u. [38,42].

We can also observe from Figs. 3(a) and 3(b) that the differences start to disappear for high electron energies, where the spectra are dominated by the rescattered electrons. This is so because the core potential plays a minor role in this energy region. Furthermore, our model captures the CEP asymmetry as well: electrons with positive final momentum are more influenced by the laser field polarization and this creates a stronger interference pattern.

2. CO *molecule*

In the CO calculation we set the parameters of our nonlocal SR potential to $\Gamma = 1$ and $\gamma = 0.09$ a.u., in order to match the ionization potential obtained with GAMESS, $I_p = 0.44$ a.u. As we already mentioned, this nonlocal SR potential only describes MOs as a composition of s states [see Fig. 3(a) inset]. On the other hand, the main advantage to using GAMESS is that it describes the MO much more accurately. Additionally, with GAMESS we have the possibility to easily model more complex molecules. The MO of the CO molecule obtained from GAMESS is a superposition of s and p states. We consider the CO molecule is in equilibrium, the internuclear distance is set to $R = 2.13$ a.u. (1.127 Å), and the molecule is oriented parallel to the laser field polarization.

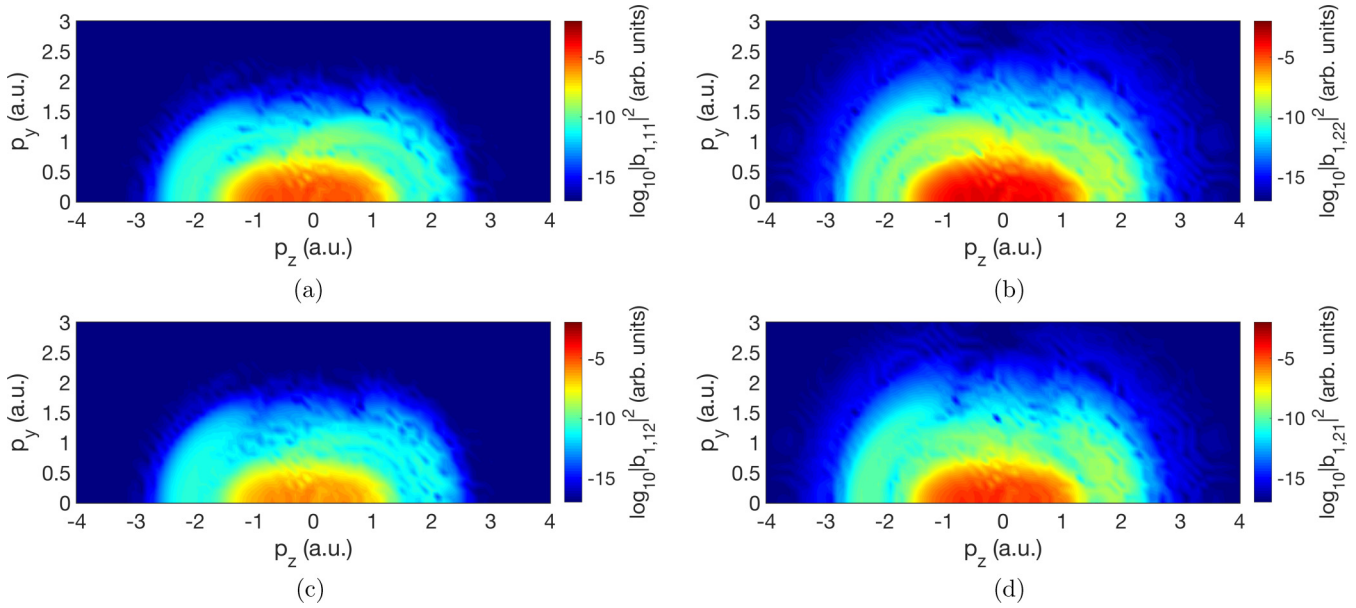

FIG. 7. Rescattering contributions to the ATI photoelectron spectra (in logarithmic scale) for a 2D-momentum plane (p_z, p_y) calculated by using model B. The CO molecule is at equilibrium, $R = 2.12$ a.u., and oriented antiparallel ($\theta = 180^\circ$) to the laser field polarization. (a) Local term of the atom on the left. (b) Local term of the atom on the right. (c) Nonlocal and cross term with ionization from the left. (d) Nonlocal and cross term with ionization from the right.

Figure 4 shows the main contributions to the final photoelectron spectra for the CO molecule: the total $|b(\mathbf{p},t)|^2$ (red solid line), the direct $|b_0(\mathbf{p},t)|^2$ (dashed with points blue line), and the rescattering $|b_1(\mathbf{p},t)|^2$ terms (black dashed line) [see Eq. (9)]. In Fig. 4(a) we display the results using model A, while the ones from model B are shown in Fig. 4(b).

A clear observation from these plots is that each term contributes to different regions of the photoelectron spectra, i.e., for electron energies $E_p \lesssim 2U_p$ the direct term $|b_0(\mathbf{p},t)|^2$ dominates the spectrum and, in contrast, it is the rescattering term $|b_1(\mathbf{p},t)|^2$ that wins in the high-energy electron region. Both photoelectron spectra show the expected two cutoffs defined by $2U_p$ and $10U_p$ (black dashed lines) which are ubiquitously present in both atomic and diatomic molecular ATI [38,42].

One of the main differences between the two models is that the total maximum yield amplitude is two orders of magnitude higher in the case of model B than in model A. Besides this contrast the dynamic ranges of the spectra are quite similar: about ten orders of magnitude until the end of the signal. Here we only show the electrons moving to the "right," i.e., with positive momentum, but as in the above case of O_2 the total spectra show CEP asymmetries.

The two spectra show some remarkable similarities; both have a deep minimum around $5U_p$, more pronounced for the model A case [Fig. 4(a)], from which the yield of the direct processes starts to decrease. The contribution of the direct processes is negligible for energies $\gtrsim 7U_p$, from which the spectra are dominated by the scattering processes. The two CO spectra show, in general, more similarities than in the O_2 case; this is due to the nature of the CO HOMO: in the CO molecule the MO is a composition of not only $2p$ but also $1s$ AOs and our SR potential is able to partially include the contribution of the latter.

In order to have a more complete picture of the underlying mechanisms we present in Fig. 5 the different direct processes contributions, $|b_0(\mathbf{p},t)|^2$, to the total ATI spectra. In Fig. 5(a) we show the split of the direct processes obtained using model A, whereas in Fig. 5(b) we depict the results using model B. The first observation in this comparison arises from the fact that the contributions from the atom on the *left* ($|b_{0,1}(\mathbf{p},t)|^2$), i.e., carbon, and the atom on the *right* ($|b_{0,2}(\mathbf{p},t)|^2$), i.e., oxygen, are different in the case of model B [Fig. 5(b)]. The amount of photoelectrons ionized from the carbon atom (pink circle line) is much larger than the one from the oxygen (yellow dashed line). This is in agreement with the shape of the CO HOMO, see Fig. 6(a), where the electronic cloud around the carbon atom is much bigger. The same effect is observed for the rescattering terms (not shown), where the total local term is dominated by the local processes coming from the carbon atom.

In the case of the calculations using model A those differences are not so pronounced [see Fig. 5(a)]: we can observe that the contributions of both atoms are equal in amplitude and shape. This is so because the bound state obtained from the SR potential does not properly describe the CO HOMO: this potential is unable to take into account the heteronuclear character of the CO molecule and describes its HOMO similar to the one shown in the inset of Fig. 3(a).

Considering the nuclear asymmetry features discussed before we next study the differences in the ATI spectra for the molecule aligned parallel (0°) or antiparallel (180°) with respect to the laser field polarization. The results of a 2D calculation, for both orientations and using the LCAO within model B, are presented in Fig. 6. Figures 6(a) and 6(c) show a sketch of the molecular orientation, superimposed over

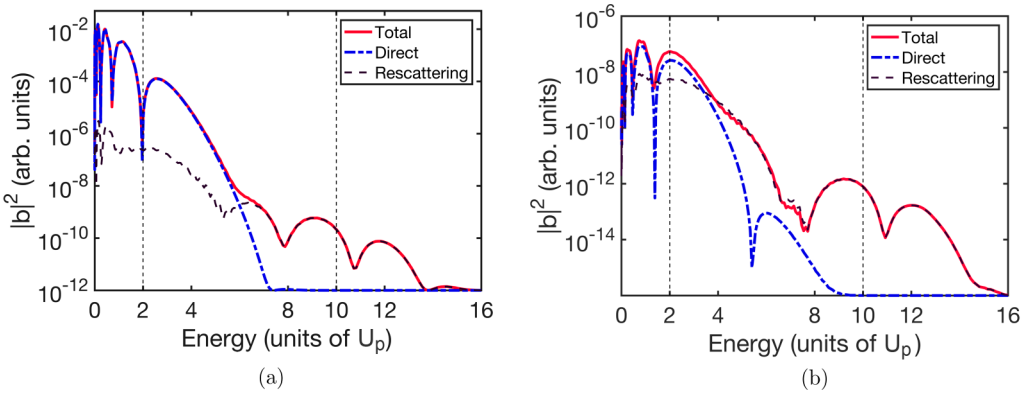

FIG. 8. CO_2 molecular ATI spectra (in logarithmic scale) as a function of the electron energy in U_p units. (a) Spectra calculated using model A. (b) Spectra computed using model B. In both calculations the CO_2 molecule is oriented perpendicular to the laser polarization (see text for more details).

the MO, formed by a combination of s and p states. Here we can see that for the case of the CO molecule aligned parallel (antiparallel) the carbon atom is on the "left" ("right"), while the oxygen atom is on the "right" ("left"). Furthermore, Figs. 6(b) and 6(d) depict the total ATI spectra for both the parallel and antiparallel cases, respectively.

The total ATI spectra presented in Figs 6(b)–6(d) show the typical CEP asymmetry, but surprisingly any features related to the heteronuclear character of the CO molecule appear to be missing: the two ATI spectra, the one obtained for the molecule at 0° [Fig. 6(b)] and the one for 180° [Fig. 6(d)], look almost identical.

In order to get a more detailed description of the CO ATI spectra presented in Figs. 6(b)–6(d), in Fig. 7 we plot the contribution of the rescattering processes to the total ATI. On the other hand, the direct contributions show the expected behavior: a symmetry inversion. In this case the major contribution also comes from the carbon atom on the *right* ($|b_{0,2}(\mathbf{p},t)|^2$), whereas the direct ionization from the oxygen atom, on the *left* ($|b_{0,1}(\mathbf{p},t)|^2$), is much smaller.

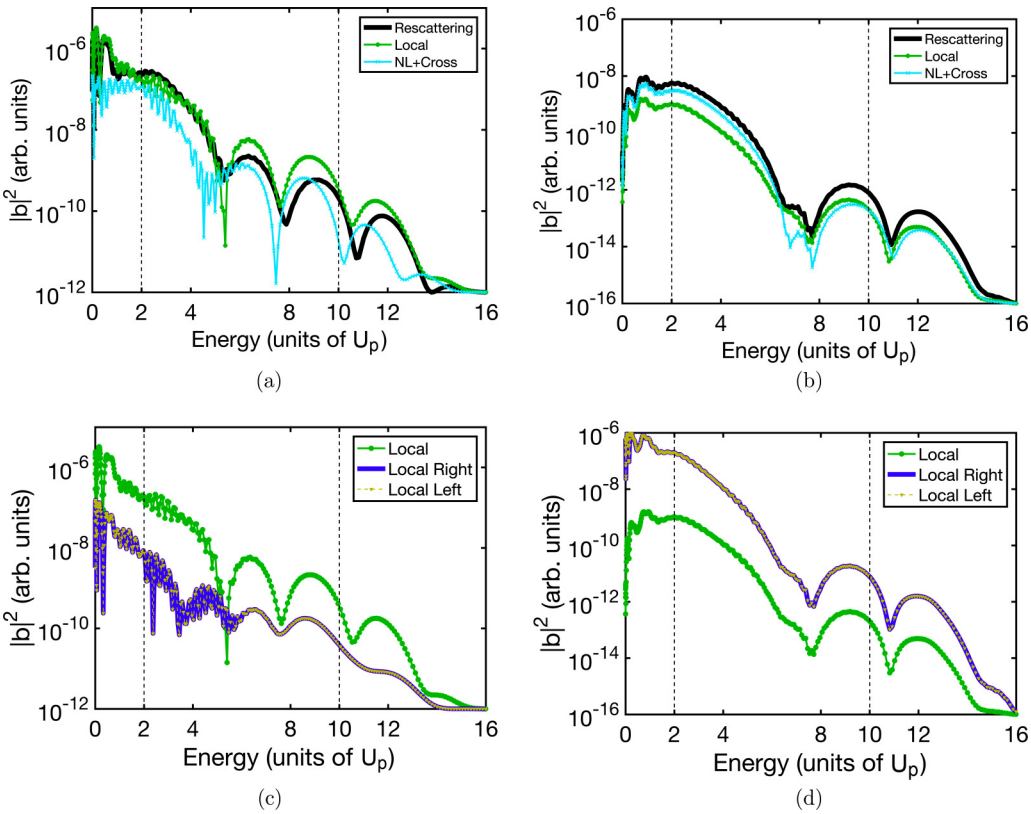

FIG. 9. Different rescattering processes contributions to the CO_2 molecular ATI spectra (in logarithmic scale) as a function of the electron energy in U_p units. (a–c) Spectra calculated using model A. (b–d) Spectra computed using model B. In both calculations the CO_2 molecule is oriented perpendicular to the laser polarization (see text for more details).

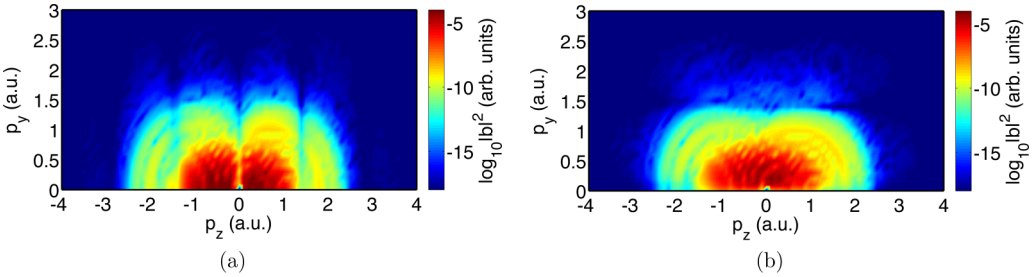

FIG. 10. 2D-total ATI photoelectron spectra (in logarithmic scale) for the CO_2 molecule as a function of the (p_z, p_y) electron momenta computed using model B. (a) The molecule is oriented parallel to the laser field polarization. (b) The same as in panel (a), but the molecule is oriented perpendicular to the laser field polarization (see text for more details).

In Figs. 7(a) and 7(b) we present the local processes contributions $|b_{1,11}(\mathbf{p},t)|^2$ and $|b_{1,22}(\mathbf{p},t)|^2$, respectively. On the other hand, Figs. 7(c) and 7(d) depict the cross and nonlocal contributions, namely, $|b_{1,12}(\mathbf{p},t)|^2$ and $|b_{1,21}(\mathbf{p},t)|^2$. In all the cases the molecule is aligned 180° with the laser field polarization, i.e., the oxygen atom is on the left, while the carbon atom is on the right. Interestingly, for the case of 0° we obtain the same plots, but with the terms interchanged, i.e., now the higher contribution comes from the carbon atom now located on the *left* at the position R_1. This is the same asymmetry feature observed in the direct terms [see Fig. 5(b)]. The heteronuclear character of the molecule can now be seen in the local and rescattering components but, as we observed, not in the total photoelectron spectra. This fact could be related to the compensation of the MO differences when the direct and rescattering terms are coherently added.

B. Results on triatomic molecules: CO_2 and CS_2

In this section we are going to extend our analysis to more complicated molecular systems, formed now by three atomic centers. We start our analysis computing the ATI for the CO_2 molecule. We present the different contributions, direct and rescattering, to the total photoelectron spectra and discuss their differences and similarities. We use next the CS_2 molecule as another three-center prototypical system. For this case we also calculate the different processes contributing to the total spectra and make a similar study to the one done for CO_2. In this way we are able to highlight both the discrepancies and coincidences between these two comparable molecular systems.

1. CO_2 *molecule*

We consider a CO_2 molecule in equilibrium, i.e., the two oxygen atoms are separated a distance $R = 4.4$ a.u. (2.327 Å) with the carbon atom located in the midpoint. The ionization potential of the outer electron predicted by GAMESS is $I_p = 0.39$ a.u. The corresponding parameters of our nonlocal SR potential to obtain this I_p are $\Gamma = 0.8$ and $\gamma = 0.1$ a.u.

In Fig. 8 we present the ATI spectra, computed by using both model A [Fig. 8(a)] and model B [Fig. 8(b)]. Here, we show the different contributions: the total $|b(\mathbf{p},t)|^2$ (solid red line), the direct $|b_0(\mathbf{p},t)|^2$ (dashed with points blue line), and the rescattering $|b_1(\mathbf{p},t)|^2$ (black dashed line) ones for each model. In both models we see that the direct processes contribute only in the low-energy region of the spectra, $E_p \lesssim 6U_p$, being negligible at high energies, where the rescattering terms are dominant. In this case we also observe an overestimation of the direct terms and a difference of four orders of magnitude in the total yield between model A [Fig. 8(a)] and model B [Fig. 8(b)]. Besides this difference in amplitude, the shapes of the spectra are quite similar: the change between direct and rescattering dominance is around the same energy ($\sim 5U_p$). However, we want to focus our attention on the high-energy part of the ATI spectra, $E_p \gtrsim 4U_p$. As can be seen, the two models show the same number of minima at around the same positions $\approx 5U_p$, $\approx 8U_p$, and $\approx 11U_p$. In order to investigate if these minima are generated by the interference between the

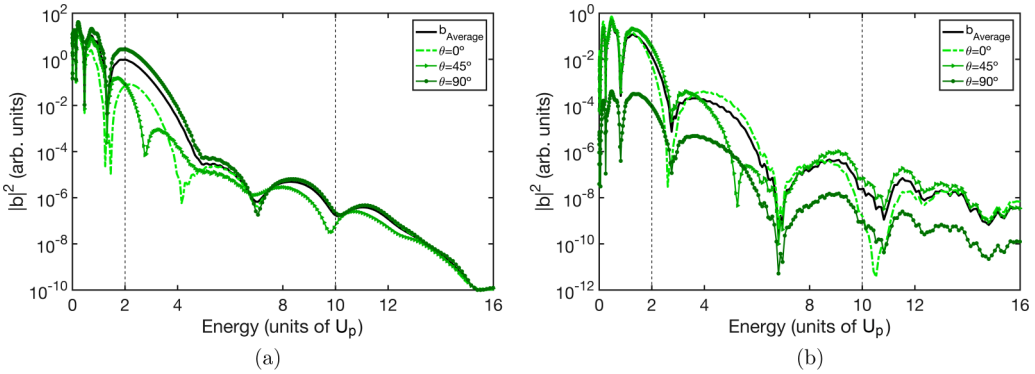

FIG. 11. Total photoelectron spectra (in logarithmic scale) as a function of the electron energy in U_p units. (a) Calculated by using model A. (b) Calculated using model B. In both models the CS_2 molecule is at equilibrium $R = 5.86$ a.u. (3.1 Å). The peak laser intensity used in this calculation is set to $I_0 = 1 \times 10^{14}$ W cm^{-2} (see text for more details).

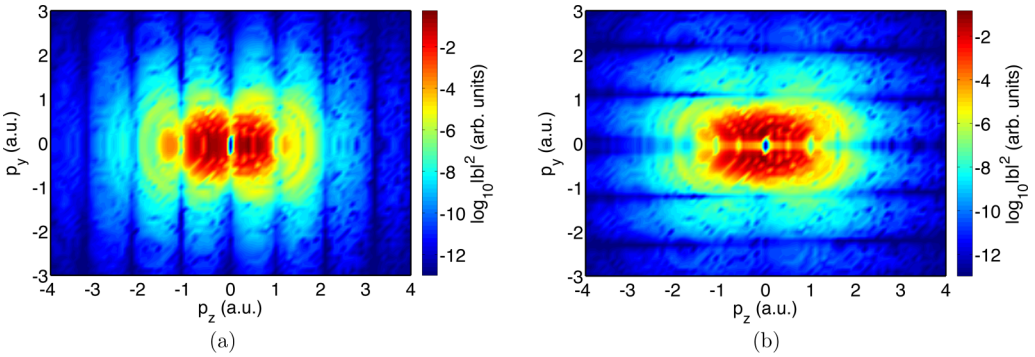

FIG. 12. 2D-total ATI photoelectron spectra (in logarithmic scale) for the CS_2 molecule as a function of the (p_z, p_y) electron momenta computed using model B. (a) The molecule is oriented parallel to the laser field polarization. (b) The same as in panel (a), but the molecule is oriented perpendicular to the laser field polarization (see text for more details).

local and nonlocal+cross terms in Fig. 9 we split the different rescattering processes' contributions.

As can be seen in Figs. 9(a) and 9(b), both local (green line with circles) and nonlocal and cross contributions (cyan line with crosses) have almost the same yield over all the electron energy range and only minor differences are visible. As a consequence the minima appear to be generated by the destructive interference between electrons tunnel ionized and rescattered in the same ion core. In Figs. 9(c) and 9(d), we present a split of the local processes, namely, $|b_{1,11}(\mathbf{p},t)|^2$ (dotted yellow line with downward-pointing triangle) and $|b_{1,33}(\mathbf{p},t)|^2$ (solid thick purple line). As we can see, the contribution from the O atoms, placed at the end of the molecule, is equal in amplitude and shape in both models. In contrast, the contribution of the C atom, placed at the origin, is almost negligible (not shown in the figure).

Regarding the deep minima, if we take a look at Figs. 9(c) and 9(d), we see that they are present in the independent contributions $|b_{1,11}(\mathbf{p},t)|^2$ and $|b_{1,33}(\mathbf{p},t)|^2$. This reinforces the hypothesis that internal interferences, inside of the atoms, are responsible for those minima. We can also observe that, in the case of model A, the local contributions (right and left) add up to enhance the total local contribution. In the case of model B, those two local contributions interfere with each other, leading to a total contribution with lower amplitude and exactly the same shape. This is a direct consequence of both the bound-state wave function and the HOMO shape.

Let us next analyze the effect of the molecular orientation on the ATI spectra. In order to do this we compute the final photoelectron spectra for the molecule oriented parallel and perpendicular with respect to the laser field polarization. In both cases we use model B and in Fig. 10 we show the results.

In the parallel configuration, $\theta = 0^\circ$ [Fig. 10(a)], we can see the typical interference pattern with deep minima located at around $p_z = \pm 1.4$ a.u. The position of these minima is in agreement with the second minimum predicted by the two slit interference formula [29] for two radiant points separated by a distance $R = 2.2$ a.u, i.e., only the separation between the oxygen and the carbon atoms. In contrast, in the perpendicular configuration, $\theta = 90^\circ$ [Fig. 10(b)], there is no trace of two-center interferences.

2. CS_2 *molecule*

For the CS_2 molecule we focus our attention on the dependency of the total photoelectron spectra on the molecular orientation. We perform calculations using both models for three different orientation angles. The parameters used in the nonlocal SR potential are $\Gamma = 0.71$ and $\gamma = 0.099$ a.u.. With these values, we match the ionization potential $I_p = 0.32$ a.u of the CS_2 molecule obtained with GAMESS. Additionally, the CS_2 HOMO is modeled in model B as a combination of only $2p$ AOs.

We consider the molecule oriented at $\theta = 0^\circ$ (light green dashed line), $\theta = 45^\circ$ (medium green solid line with right-pointing triangle), and $\theta = 90^\circ$ (dark green solid line with circles) with respect to the laser field polarization and we also include an averaged-ATI spectra (solid black line) over these three orientations.

The calculations using model A [Fig. 11(a)] show only minor dissimilarities in shape and amplitude for the three different orientations. The main differences appear in the low-energy part, where the spectra depict different yields and the positions of the interference minima change. In this case the most favorable orientation, i.e., the one that gives the highest yield, is $\theta = 90^\circ$ (dark green solid line with circles), i.e., the molecule is oriented perpendicular to the laser field polarization. This result is in agreement with our previous publication [31], where the HHG for a three-center molecule, CO_2, shows a similar behavior.

For the ATI spectra obtained using model B [Fig. 11(b)], we observe that the behavior is completely the opposite: in the perpendicular case (dark green solid line with circles) the total yield drops by more than three orders of magnitude and it is the parallel orientation (light green dashed line) that dominates. Additionally, the differences between the three orientations are now more visible. We could argue then that model B is not only more accurate in the MO description but also more sensitive to the molecular orientation.

In order to discuss differences and similarities with the CO_2 case, in Fig. 12 we present 2D-total photoelectron spectra for a CS_2 molecule oriented at $\theta = 0^\circ$ [Fig. 12(a)] and $\theta = 90^\circ$ [Fig. 12(b)], with respect to the laser field polarization.

The results obtained show the sensitivity of our model to the molecular orientation and the presence of interference minima now for the two orientations [this is in clear contrast to the CO_2 case, where for the perpendicular orientation, Fig. 10(b), there are not fingerprints of interferences]. Furthermore, we observe that, for the parallel case, Fig. 12(a), the interference minima are placed for fixed p_z values, i.e., parallel to the p_y axis, while for the case of $\theta = 90^\circ$ these minima are for fixed p_y values, i.e., parallel to the p_z axis. These features are related to the shape of the CS_2 HOMO, that is inherited in the molecular bound-free matrix element.

V. CONCLUSIONS AND OUTLOOK

Before concluding, we would like to discuss with more detail the similarities and differences between the generalized SFA, used in this paper, and the independent-atom model (IAM) used in diffraction theory and recently also in LIED (see, for example, [43]). At first glance, both approaches have some similarities. However, there are also significant differences. In LIED, the IAM is used only for returning electrons with sufficiently high energies and large scattering angles, whereas in the present theory there is no such restriction.

The IAM is based on the following basic assumptions.

(1) It neglects the bound-states structure of the target.

(2) Electron rescattering is treated here in a process similar to scattering by laboratory prepared electrons. Electrons are described thus as incoming plane waves (alternatively wave packets of superimposed plane waves).

(3) Scattering on the target in many cases may be calculated using the Born perturbation theory but, if needed, can be calculated using more sophisticated approximations of the scattering theory, or even calculated exactly. The IAM is quite precise for electrons of high energies (say 5–$10U_p$).

(4) It focuses on high-energy angle-resolved photoelectron spectra of molecules in strong fields.

(5) The IAM does not consider the dynamics of the initial tunneling process and, thus, does apply to the electrons undergoing direct ionization. In fact, it is well known that the description of these active directly ionized electrons (normally valence electrons) by the IAM is quite inaccurate.

In contrast, generalized SFA is a systematic approximate solution of the TDSE, based on the following assumptions.

(1) Like the IAM, it neglects the bound-states structure of the target, except for its ground state.

(2) It treats electron continuum-continuum transitions (scattering) in a perturbative way. In the zeroth order, the electron's dynamics is described by the Volkov action.

(3) The generalized SFA treats the laser field nonperturbatively.

(4) Electrons' dynamics in the continuum is similar to that corresponding to plane waves, as in the IAM, but here we deal with the Volkov waves, dressed in the laser field.

(5) In the zeroth order, the generalized SFA (known also as the Keldysh-Faisal-Reiss model [34–36]) describes quite well direct tunnel ionization of electrons that never return to the target; they have energies between zero and $2U_p$. Typically, good agreement with the TDSE and experiments is achieved for electrons of energies larger than I_p. For the intensities considered here we have $I_p \leqslant U_p$ and this corresponds to electrons with energies, say $U_p < E < 2U_p$.

(6) In the first order, the generalized SFA treats the rescattering processes perturbatively with respect to the continuum-continuum matrix element, describing scattering on the target in the presence of the laser field. The IAM might be more precise in treating the scattering itself, but is less accurate in treating the laser field effects, which are evidently important for electrons of moderate energies, say around $2U_p$.

(7) Rescattered electrons may reach energies up to typically $10U_p$ (although this depends on laser polarization, etc.).

(8) Each contribution to the spectrum and angular distribution of electrons has quasiclassical interpretation in terms of quasiclassical (complex) trajectories (for the foundations of HHG and ATI see [32,38], respectively). Contributions corresponding to individual trajectories are calculated in the generalized SFA very precisely (see [15]). The fragile interference between the different trajectories, leading for instance to the rings in the ATI and involving both direct and rescattered electrons, is also reproduced by the generalized SFA qualitatively [38], but not so well quantitatively. In most of the experiments, these interference effects, however, are often averaged out by the spatial distribution of intensity in the pulse and temporal effects.

In short, the advantage of the generalized SFA over the IAM is that SFA can handle electrons of energies $E > U_p \leqslant I_p$ and includes the laser dressing exactly. The disadvantage is that the rescattering process is treated in the laser-dressed Born approximation, whereas in the IAM it can be tackled, in principle, exactly.

In a similar vein, it is also important to remark that the generalized SFA has a limited inclusion of Coulomb effects (though it can be extended in the direction of the Coulomb-Volkov approximation [44]), and this can limit the approximation's accuracy to some extent. The inclusion of Coulomb effects into descriptions of ionization is an active area of research [45] through a wide array of methods, including, e.g., the Coulomb-corrected SFA [46] and the analytical R-matrix theory [47–49], but generally speaking the more Coulomb effects are included the less analytical and manageable the theory becomes, requiring either "shotgun" trajectory approaches [46] or an increased overhead on the description of recollisions [48]. In the generalized SFA we present here, we prioritize the handling of multicenter systems within an analytical framework, which can then be adapted to include Coulomb effects once the atomic picture becomes clearer.

Summarizing, we presented a quasiclassical approach that deals with molecular ATI within the SAE approximation. Our model could be considered as a natural extension to the one introduced in [29,30]. The focus of the present paper is on triatomic molecular systems, although the extension to more complex systems appears to be straightforward.

First, we have shown our approach is able to capture the interference features ubiquitously present in every molecular ATI process. As was already described, the cores of our model are the saddle-point approximation and the LCAO. One of the main advantages of our approach is the possibility to disentangle, in an easy and direct way, the different contributions to the total ATI. This is particularly important for complex systems, where there exists a large amount of direct and

rescattering "scenarios" that otherwise would be impossible to extricate.

Second, we establish a comparison using two different ground states, one that uses a nonlocal SR potential, model A, and the other based on the LCAO, model B. While both models allow us to formulate the ATI in a semianalytical way, the latter (model B) gives a more accurate description of the MO. Nevertheless, we proved that, even when the former (model A) predicts an overestimation of the direct processes, the shape and the spectra features are well reproduced. Additionally, model B appears to be the adequate platform to investigate much more complex systems. For instance, the modeling of the DNA basis, formed by around 12 atoms, seems to be perfectly feasible. This will be the object of future investigations.

ACKNOWLEDGMENTS

This paper was supported by the project Extreme Light Infrastructure phase 2 (Grant No. CZ.02.1.01/0.0/0.0/15_008/0000162) from European Regional Development Fund, Ministerio de Economía y Competitividad through Plan Nacional (Grant No. FIS2016-79508-P, FISICATEAMO, and Severo Ochoa Excellence Grant No. SEV-2015-0522), and funding from the European Unions Horizon 2020 research and innovation program under the Marie Sklodowska-Curie Grant No. 641272 and Laserlab-Europe (Grant No. EU-H2020 654148), Fundació Privada Cellex, and Generalitat de Catalunya (Grant No. SGR 1341 and CERCA program). N.S. was supported by the Erasmus Mundus Doctorate Program Europhotonics (Grant No. 159224-1-2009-1-FR-ERAMUNDUS-EMJD). N.S., A.C., E.P., and M.L. acknowledge European Research Council AdG OSYRIS, European Union FETPRO QUIC, and National Science Centre Poland-Symfonia Grant No. 2016/20/W/ST4/00314. J.B. acknowledges Grants No. FIS2017-89536-P, 2017 SGR 1639, Laserlab-Europe (EU-H2020 654148), and the Polish National Science Center within the grant Poland-Symfonia No. 2016/20/W/ST4/00314. This project has received funding from the European Union's Horizon 2020 research and innovation programme under the Marie Sklodowska-Curie Grant Agreement No. 702565 and TALENTO grant from Comunidad de Madrid ref. 2017-T1/IND-5432. We thank Robert Moszynski, Kuba Zakrzewski, and Francesca Calegari for fruitful discussions.

APPENDIX: TWO-CENTER SYSTEMS—BOUND-CONTINUUM AND RESCATTERING TRANSITION MATRIX ELEMENTS

In this Appendix we present the equations to calculate the bound-continuum and the rescattering matrix elements for a diatomic molecule. In this case we set $n = 2$ where n determines the number of atoms, in such a way to distinguish this formulation from the one presented for three-center systems.

Let us first recall the expression for the bound state of a diatomic system obtained in [29], i.e.,

$$\Psi_{2-0_{\rm SR}}(\mathbf{p}) = \frac{\mathcal{M}_2\, e^{-i\mathbf{R}_1\cdot\mathbf{p}}}{\sqrt{(p^2+\Gamma^2)}\left(\frac{p^2}{2}+I_p\right)} + \frac{\mathcal{M}_2\, e^{-i\mathbf{R}_2\cdot\mathbf{p}}}{\sqrt{(p^2+\Gamma^2)}\left(\frac{p^2}{2}+I_p\right)}, \tag{A1}$$

where the normalization constant $\mathcal{M}_2$ is

$$\mathcal{M}_2 = \frac{1}{2}\left[\frac{2\pi^2}{(2I_p-\Gamma^2)^2}\left\{\frac{2\,e^{-R\Gamma}}{R} - \frac{2\,e^{-R\sqrt{2I_p}}}{R} - \frac{(2I_p-\Gamma^2)e^{-R\sqrt{2I_p}}}{\sqrt{2I_p}} + \frac{(\sqrt{2I_p}-\Gamma)^2}{\sqrt{2I_p}}\right\}\right]^{-1/2}. \tag{A2}$$

Following the definition in Eq. (13), with now $n = 2$, we have

$$\mathbf{d}_{2-\rm SR}(\mathbf{p}_0) = \sum_{j=1}^{2}\mathbf{d}_{2-{\rm SR}_j}(\mathbf{p}_0) = -2i\,\mathcal{M}_2\mathcal{A}(\mathbf{p}_0)\,\{e^{-i\mathbf{R}_1\cdot\mathbf{p}_0} + e^{-i\mathbf{R}_2\cdot\mathbf{p}_0}\}, \tag{A3}$$

where $\mathcal{A}(\mathbf{p}_0)$ is defined as

$$\mathcal{A}(\mathbf{p}_0) = -\mathbf{p}_0\,\frac{\left(3p_0^2+2I_p+2\Gamma^2\right)}{\left(p_0^2+\Gamma^2\right)^{\frac{3}{2}}\left(p_0^2+2I_p\right)^2}. \tag{A4}$$

Using this last equation we have completely defined the direct transition amplitude for a two-center system by inserting Eq. (A3) in Eq. (5).

For the calculation of the rescattering and the total transition amplitudes we need to obtain the scattering states and the rescattering transition matrix elements. In this way, the scattering state reads as

$$\Psi_{2-\mathbf{p}_0} = \delta(\mathbf{p}-\mathbf{p}_0) + \sum_{j=1}^{2}\delta\Psi_{2-\mathbf{R}_j\mathbf{p}_0}(\mathbf{p}), \tag{A5}$$

where

$$\delta\Psi_{2-\mathbf{R}_1\mathbf{p}_0}(\mathbf{p}) = \frac{\mathcal{D}_{2\,-\,1}(\mathbf{p}_0)\,e^{-i\mathbf{R}_1\cdot(\mathbf{p}\,-\,\mathbf{p}_0)} - \mathcal{D}_{2-2}(\mathbf{p}_0)\,e^{-i\mathbf{R}_1\cdot(\mathbf{p}\,+\,\mathbf{p}_0)}}{\sqrt{p^2+\Gamma^2}\,\left(p_0^2-p^2+i\epsilon\right)}, \tag{A6}$$

$$\delta\Psi_{2-\mathbf{R}_2\mathbf{p}_0}(\mathbf{p}) = \frac{\mathcal{D}_{2\,-\,1}(\mathbf{p}_0)\,e^{-i\mathbf{R}_2\cdot(\mathbf{p}\,-\,\mathbf{p}_0)} - \mathcal{D}_{2\,-\,2}(\mathbf{p}_0)\,e^{-i\mathbf{R}_2\cdot(\mathbf{p}\,+\,\mathbf{p}_0)}}{\sqrt{p^2+\Gamma^2}\,\left(p_0^2-p^2+i\epsilon\right)}. \tag{A7}$$

Finally, let us obtain the explicit expressions for the rescattering transition matrix elements for diatomics, $\mathbf{g}_{2-jj'}$:

$$\mathbf{g}_{2-11}(\mathbf{p}_1,\mathbf{p}_2) = \mathcal{Q}_{2-1}(\mathbf{p}_1,\mathbf{p}_2)\, e^{-i\mathbf{R}_1\cdot(\mathbf{p}_1-\mathbf{p}_2)}, \quad \mathbf{g}_{2-12}(\mathbf{p}_1,\mathbf{p}_2) = \mathcal{Q}_{2-2}(\mathbf{p}_1,\mathbf{p}_2)\; e^{-i\mathbf{R}_2\cdot\mathbf{p}_1+i\mathbf{R}_1\cdot\mathbf{p}_2},$$
$$\mathbf{g}_{2-22}(\mathbf{p}_1,\mathbf{p}_2) = \mathcal{Q}_{2-1}(\mathbf{p}_1,\mathbf{p}_2)\, e^{-i\mathbf{R}_2\cdot(\mathbf{p}_1-\mathbf{p}_2)}, \quad \mathbf{g}_{2-21}(\mathbf{p}_1,\mathbf{p}_2) = \mathcal{Q}_{2-2}(\mathbf{p}_1,\mathbf{p}_2)\, e^{-i\mathbf{R}_1\cdot\mathbf{p}_1+i\mathbf{R}_2\cdot\mathbf{p}_2}, \tag{A8}$$

where

$$\mathcal{Q}_{2-1}(\mathbf{p}_1,\mathbf{p}_2) = i[\mathcal{D}_{2-1}(\mathbf{p}_2)\mathcal{C}_1(\mathbf{p}_1,\mathbf{p}_2) - \mathcal{D}^*_{2_1}(\mathbf{p}_1)\mathcal{C}_2(\mathbf{p}_1,\mathbf{p}_2)] \tag{A9}$$

and

$$\mathcal{Q}_{2-2}(\mathbf{p}_1,\mathbf{p}_2) = -i[\mathcal{D}_{2-2}(\mathbf{p}_2)\mathcal{C}_1(\mathbf{p}_1,\mathbf{p}_2) - \mathcal{D}^*_{2-2}(\mathbf{p}_1)\mathcal{C}_2(\mathbf{p}_1,\mathbf{p}_2)]. \tag{A10}$$

The functions in Eqs. (A9) and (A10) are defined as

$$\mathcal{D}_{2-1}(\mathbf{p}_0) = \frac{\gamma}{\sqrt{p_0^2+\Gamma^2}}\left\{\frac{1+I_1'}{I_2'^2-(1+I_1')^2}\right\}, \quad \mathcal{D}_{2-2}(\mathbf{p}_0) = \frac{\gamma}{\sqrt{p_0^2+\Gamma^2}}\left\{\frac{I_2'}{I_2'^2-(1+I_1')^2}\right\}, \tag{A11}$$

$$I_1' = \frac{-2\pi^2\,\gamma}{\Gamma - i\sqrt{|p_0^2+i\,\epsilon|}}, \tag{A12}$$

$$I_2' = \frac{-2\pi^2\,\gamma}{R\left(p_0^2+\Gamma^2+i\epsilon\right)}[e^{i\,R\,\sqrt{p_0^2+i\epsilon}} - e^{-R\,\Gamma}] \tag{A13}$$

and

$$\mathcal{C}_1(\mathbf{p}_1,\mathbf{p}_2) = \left[\frac{\mathbf{p}_1\left(3p_1^2-p_2^2+2\Gamma^2\right)}{\left(p_1^2+\Gamma^2\right)^{\frac{3}{2}}\left(p_2^2-p_1^2+i\epsilon\right)^2}\right], \quad \mathcal{C}_2(\mathbf{p}_1,\mathbf{p}_2) = \left[\frac{\mathbf{p}_2\left(3p_2^2-p_1^2+2\Gamma^2\right)}{\left(p_2^2+\Gamma^2\right)^{\frac{3}{2}}\left(p_1^2-p_2^2-i\epsilon\right)^2}\right]. \tag{A14}$$

[1] S. Patchkovskii, Z. Zhao, T. Brabec, and D. M. Villeneuve, High Harmonic Generation and Molecular Orbital Tomography in Multielectron Systems: Beyond the Single Active Electron Approximation, Phys. Rev. Lett. **97**, 123003 (2006).

[2] J. Itatani, J. Levesque, D. Zeidler, H. Niikura, H. Pépin, J. C. Kieffer, P. B. Corkum, and D. M. Villeneuve, Tomographic imaging of molecular orbitals, Nature (London) **432**, 867 (2004).

[3] G. N. Gibson and J. Biegert, Influence of orbital symmetry on high-order-harmonic generation and quantum tomography, Phys. Rev. A **78**, 033423 (2008).

[4] S. Odžak and D. B. Milošević, Interference effects in high-order harmonic generation by homonuclear diatomic molecules, Phys. Rev. A **79**, 023414 (2009).

[5] A. Li, J. Wang, N. Ren, P. Wang, W. Zhu, X. Li, R. Hoehn, and S. Kais, The interference effect of laser-assisted bremsstrahlung emission in coulomb fields of two nuclei, J. Appl. Phys. **114**, 124904 (2013).

[6] M. Qin, X. Zhu, K. Liu, Q. Zhang, and P. Lu, Imprints of the molecular-orbital geometry on the high-harmonic ellipticity, Opt. Express **20**, 20181 (2012).

[7] S. Odžak and D. B. Milošević, Dressed-bound-state molecular strong-field approximation: Application to high-order harmonic generation by heteronuclear diatomic molecules, J. Opt. Soc. Am. B **29**, 2147 (2012).

[8] N. Nguyen and V. Le, Retrieval of interatomic separations of complex molecules by ultra-short laser pulses, Comput. Theor. Chem. **964**, 12 (2011).

[9] E. Hijano, C. Serrat, G. N. Gibson, C. F. de Morisson Faria, and J. Biegert, Retrieval of interatomic separations of complex molecules by ultra-short laser pulses, J. Mod. Opt. **58**, 1166 (2011).

[10] C. F. de Morisson Faria and B. B. Augstein, Molecular high-order harmonic generation with more than one active orbital: Quantum interference effects, Phys. Rev. A **81**, 043409 (2010).

[11] E. Hijano, C. Serrat, G. N. Gibson, and J. Biegert, Orbital geometry determined by orthogonal high-order harmonic polarization components, Phys. Rev. A **81**, 041401 (2010).

[12] T. Zuo, A. D. Bandrauk, and P. B. Corkum, Laser-induced electron diffraction: A new tool for probing ultrafast molecular dynamics, Chem. Phys. Lett. **259**, 313 (1996).

[13] M. Lein, J. P. Marangos, and P. L. Knight, Electron diffraction in above-threshold ionization of molecules, Phys. Rev. A **66**, 051404 (2002).

[14] C. D. Lin, A. T. Le, Z. Chen, T. Morishita, and R. Lucchese, Strong-field re-scattering physics-self-imaging of a molecule by its own electrons, J. Phys. B **43**, 122001 (2010).

[15] P. Salières, B. Carré, L. L. Déroff, F. Grasbon, G. G. Paulus, H. Walther, R. Kopold, W. Becker, D. B. Milošević, A. Sanpera, and M. Lewenstein, Feynman's path-integral approach for intense-laser-atom interactions, Science **292**, 902 (2001).

[16] J. Xu, C. I. Blaga, K. Zhang, Y. H. Lai, C. D. Lin, T. A. Miller, P. Agostini, and L. F. DiMauro, Diffraction using laser-driven broadband electron wave packets, Nat. Commun. **5**, 4635 (2014).

[17] C. I. Blaga, J. Xu, A. D. DiChiara, E. Sistrunk, K. Zhang, P. Agostini, T. A. Miller, L. F. DiMauro, and C. D. Lin, Imaging ultrafast molecular dynamics with laser-induced electron diffraction, Nature (London) **483**, 194 (2012).

[18] M. G. Pullen, B. Wolter, A. T. Le, M. Baudisch, M. Hemmer, A. Senftleben, C. D. Schröter, J. Ullrich, R. Moshammer, C. D.

Lin *et al.*, Imaging an aligned polyatomic molecule with laser-induced electron diffraction, Nat. Commun. **6**, 7262 (2015).
[19] B. Wolter, M. G. Pullen, A. T. Le, M. Baudisch, K. Doblhoff-Dier, A. Senftleben, M. Hemmer, C. D. Schröter, J. Ullrich, T. Pfeifer, R. Moshammer, S. Gräfe, O. Vendrell, C. D. Lin, and J. Biegert, Ultrafast electron diffraction imaging of bond breaking in di-ionized acetylene, Science **354**, 308 (2016).
[20] C. C. Chirilă and M. Lein, Strong-field approximation for harmonic generation in diatomic molecules, Phys. Rev. A **73**, 023410 (2006).
[21] H. Hetzheim, C. F. de Morisson Faria, and W. Becker, Interference effects in above-threshold ionization from diatomic molecules: Determining the internuclear separation, Phys. Rev. A **76**, 023418 (2007).
[22] M. Lein, Molecular imaging using recolliding electrons, J. Phys. B **40**, R135 (2007).
[23] E. V. van der Zwan and M. Lein, Molecular Imaging Using High-Order Harmonic Generation and Above-Threshold Ionization, Phys. Rev. Lett. **108**, 043004 (2012).
[24] D. B. Milošević, Strong-field approximation for ionization of a diatomic molecule by a strong laser field, Phys. Rev. A **74**, 063404 (2006).
[25] M. Busuladžić, A. Gazibegović-Busuladžić, D. B. Milošević, and W. Becker, Angle-Resolved High-Order Above-Threshold Ionization of a Molecule: Sensitive Tool for Molecular Characterization, Phys. Rev. Lett. **100**, 203003 (2008).
[26] K.-J. Yuan and A. D. Bandrauk, Symmetry in circularly polarized molecular high-order harmonic generation with intense bicircular laser pulses, Phys. Rev. A **97**, 023408 (2018).
[27] M. F. Ciappina, C. C. Chirilă, and M. Lein, Influence of coulomb continuum wave functions in the description of high-order harmonic generation with H_2^+, Phys. Rev. A **75**, 043405 (2007).
[28] M. F. Ciappina and W. R. Cravero, Two center and coulomb effects in near-threshold ionization of H_2^+ by short laser pulses, J. Mod. Opt. **56**, 11 (2009).
[29] N. Suárez, A. Chacón, M. F. Ciappina, B. Wolter, J. Biegert, and M. Lewenstein, Above-threshold ionization and laser-induced electron diffraction in diatomic molecules, Phys. Rev. A **94**, 043423 (2016).
[30] N. Suárez, A. Chacón, M. F. Ciappina, J. Biegert, and M. Lewenstein, Above-threshold ionization and photoelectron spectra in atomic systems driven by strong laser fields, Phys. Rev. A **92**, 063421 (2015).
[31] N. Suárez, A. Chacón, J. A. Pérez-Hernández, J. Biegert, M. Lewenstein, and M. F. Ciappina, High-order-harmonic generation in atomic and molecular systems, Phys. Rev. A **95**, 033415 (2017).
[32] M. Lewenstein, Ph. Balcou, M. Y. Ivanov, A. L'Huillier, and P. B. Corkum, Theory of high-harmonic generation by low-frequency laser fields, Phys. Rev. A **49**, 2117 (1994).
[33] M. Busuladžić, A. Gazibegović-Busuladžić, D. B. Milošević, and W. Becker, Strong-field approximation for ionization of a diatomic molecule by a strong laser field. II: The role of electron rescattering off the molecular centers, Phys. Rev. A **78**, 033412 (2008).
[34] L. V. Keldysh, Ionization in the field of a strong electromagnetic wave, ZhETF **47**, 1945 (1965) [Sov. Phys. JETP **20**, 1307 (1965)].
[35] F. H. M. Faisal, Multiple absorption of laser photons by atoms, J. Phys. B **6**, L89 (1973).
[36] H. R. Reiss, Effect of an intense electromagnetic field on a weakly bound system, Phys. Rev. A **22**, 1786 (1980).
[37] J. Grochmalicki, J. R. Kukliński, and M. Lewenstein, Above-threshold ionisation and electron scattering in intense laser fields, J. Phys. B **19**, 3649 (1986).
[38] M. Lewenstein, K. C. Kulander, K. J. Schafer, and P. H. Bucksbaum, Rings in above-threshold ionization: A quasiclassical analysis, Phys. Rev. A **51**, 1495 (1995).
[39] M. W. Schmidt, K. K. Baldridge, J. A. Boatz, S. T. Elbert, M. S. Gordon, J. H. Jensen, S. Koseki, N. Matsunaga, K. A. Nguyen, S. J. Su, T. L. Windus, M. Dupuis, and J. A. Montgomery, General atomic and molecular electronic structure system, J. Comput. Chem. **14**, 1347 (1993).
[40] M. S. Gordon and M. W. Schmidt, Advances in Electronic Structure Theory: Gamess a Decade Later, in *Theory and Applications of Computational Chemistry, the first forty years*, edited by C. E. Dykstra, G. Frenking, K. S. Kim, and G. E. Scuseria (Elsevier, Amsterdam, 2005), pp. 1167–1189.
[41] B. Chapman, G. Jost, and R. Van Der Pas, *Using OpenMP: Portable Shared Memory Parallel Programming* (MIT, Cambridge, MA, 2007).
[42] D. B. Milošević, G. G. Paulus, D. Bauer, and W. Becker, Above-threshold ionization by few-cycle pulses, J. Phys. B **39**, R203 (2006).
[43] J. Xu, Z. Chen, A.-T. Le, and C. D. Lin, Self-imaging of molecules from diffraction spectra by laser-induced rescattering electrons, Phys. Rev. A **82**, 033403 (2010).
[44] D. G. Arbó, J. E. Miraglia, M. S. Gravielle, K. Schiessl, E. Persson, and J. Burgdörfer, Coulomb-Volkov approximation for near-threshold ionization by short laser pulses, Phys. Rev. A **77**, 013401 (2008).
[45] S. V. Popruzhenko, Keldysh theory of strong field ionization: History, applications, difficulties and perspectives, J. Phys. B **47**, 204001 (2014).
[46] Y. Huismans, A. Rouzée, A. Gijsbertsen, J. H. Jungmann, A. S. Smolkowska, P. S. W. M. Logman, F. Lepine, C. Cauchy, S. Zamith, T. Marchenko *et al.*, Time-resolved holography with photoelectrons, Science **331**, 61 (2011).
[47] L. Torlina and O. Smirnova, Time-dependent analytical *R*-matrix approach for strong-field dynamics. I: One-electron systems, Phys. Rev. A **86**, 043408 (2012).
[48] E. Pisanty and M. Ivanov, Slalom in complex time: Emergence of low-energy structures in tunnel ionization via complex-time contours, Phys. Rev. A **93**, 043408 (2016).
[49] Th. Keil, S. V. Popruzhenko, and D. Bauer, Laser-Driven Recollisions Under the Coulomb Barrier, Phys. Rev. Lett. **117**, 243003 (2016).